

RESEARCH ARTICLE

Material modeling for parametric, anisotropic finite strain hyperelasticity based on machine learning with application in optimization of metamaterials

Mauricio Fernández^{1,2}  | Felix Fritzen³  | Oliver Weeger¹ 

¹Cyber-Physical Simulation, Technical University of Darmstadt, Darmstadt, Germany

²Multiscale and Data-Driven Material Modeling, ACCESS e.V., Aachen, Germany

³Data Analytics in Engineering, University of Stuttgart, Stuttgart, Germany

Correspondence

Mauricio Fernández, Cyber-Physical Simulation, Technical University of Darmstadt, Darmstadt, Germany.

Email:

m.fernandez@access-technology.de

Funding information

Deutsche Forschungsgemeinschaft, Grant/Award Numbers: 390740016 / EXC-2075, 406068690 / FR2702/8

Abstract

Mechanical metamaterials such as open- and closed-cell lattice structures, foams, composites, and so forth can often be parametrized in terms of their microstructural properties, for example, relative densities, aspect ratios, material, shape, or topological parameters. To model the effective constitutive behavior and facilitate efficient multiscale simulation, design, and optimization of such parametric metamaterials in the finite deformation regime, a machine learning-based constitutive model is presented in this work. The approach is demonstrated in application to elastic beam lattices with cubic anisotropy, which exhibit highly nonlinear effective behaviors due to microstructural instabilities and topology variations. Based on microstructure simulations, the relevant material and topology parameters of selected cubic lattice cells are determined and training data with homogenized stress-deformation responses is generated for varying parameters. Then, a parametric, hyperelastic, anisotropic constitutive model is formulated as an artificial neural network, extending a recent work of the author extending a recent work of the author, *Comput Mech.*, 2021;67(2):653-677. The machine learning model is calibrated with the simulation data of the parametric unit cell. The authors offer public access to the simulation data through the GitHub repository <https://github.com/CPShub/sim-data>. For the calibration of the model, a dedicated sample weighting strategy is developed to equally consider compliant and stiff cells and deformation scenarios in the objective function. It is demonstrated that this machine learning model is able to represent and predict the effective constitutive behavior of parametric lattices well across several orders of magnitude. Furthermore, the usability of the approach is showcased by two examples for material and topology optimization of the parametric lattice cell.

KEYWORDS

anisotropic finite strain hyperelasticity, artificial neural networks, machine learning, material and topology optimization, parametric lattice metamaterials

1 | INTRODUCTION

Metamaterials offer today a wide spectrum of tunable mechanical, thermal, optical, acoustic, and electromagnetic properties, see, for example, References 1,2. Thus, typically, families of parametric metamaterials are developed and investigated in order to tailor their specific functionality controlled by material, geometric, or topological design parameters of the unit cell, see, for example, References 3,4. Inclusion of parameter-dependence in *linear* elastic effective constitutive models for metamaterials, foams, composites, and so forth has already been greatly exploited for multiscale simulation and optimization approaches, compare References 5-9. However, in recent years, also soft, compliant, flexible mechanical metamaterials with multi-functional capabilities have been developed, see, for example, References 10-15. To enable efficient simulations of macroscopic structures and to optimize mechanical properties related to the underlying unit cells of those metamaterials, nonlinear material models are required, which should consider the specific material symmetries and parametric dependencies of the microstructures. However, nonlinear and anisotropic constitutive modeling at finite deformations is, in general, much more challenging and representation of parameter-dependence is less explored in this context.

In particular, open-cell foams, that is, truss- or beam-based lattice metamaterials, exhibit highly nonlinear effective mechanical behavior due to microstructural instabilities (strut buckling) and tension- or bending-dominated unit cell topologies, see, for example, Reference 16. In this context of nonlinear metamaterials with instabilities, the material response is, strictly speaking, not unique due to the dependency on the manifesting instability. Still, for many applications, pragmatic approaches based on path-independent, that is, state-dependent material models show excellent agreement with experiments and simulations. For instance, a parametric hyperelastic constitutive model for honeycomb-like and re-entrant 2D lattices was developed in Reference 17 and a nonlinear micropolar continuum model with an incremental representation of the constitutive behavior was proposed in Reference 18. In References 19,20, also generalized state-dependent continuum formulations were employed for multiscale modeling of 2D and 3D beam lattices subject to finite deformations, however, in a concurrent, FE² setting without an explicit representation of the effective constitutive relationship between macro- and microscales. Thus, for efficient multiscale simulation and optimization, compare Reference 21, it is of great importance to develop generic material models that can represent the constitutive behavior of nonlinear, anisotropic metamaterials and include their parametric dependencies. An attempt to highly nonlinear structural optimization in the presence of nonlinear path-dependent microstructured materials was proposed in Reference 22 using GPU-accelerated reduced order models (ROM) to boost the efficiency of the nonlinear microscale problem.

In recent years, a wide variety of highly flexible material models based on modern data-driven and machine learning methods have pushed forward the boundaries of constitutive modeling. In the field of isotropic and anisotropic hyperelasticity, novel approaches have been developed by fitting either strain energy densities or stresses obtained from microstructural simulations and interpolating or approximating response surfaces. For instance, Reference 23 introduced a neural network approach for the approximation of nonlinear hyperelastic behavior at small deformations. In Reference 24 a polynomial ansatz was developed for the identification of the constitutive manifold, but also only at small deformations. Using ROM to generate large scale datasets allowed to identify rapid feedforward neural networks in Reference 25, where an adaptive switch between the more robust ROM and the computationally more efficient ANN allowed the resulting surrogate model to extrapolate also outside of the training range. An approach for finite hyperelasticity was developed in Reference 26 through a model-free ansatz, but showcased only for one- and two-dimensional problems with isotropic behavior. Material anisotropy was considered in Reference 27 for cubic Nickel through machine learning approaches based on data augmentation and group invariants, but without illustration of the actual nonlinear material behavior. A neural network model accounting for the isotropy of the material has been introduced in Reference 28: any data sample from the training is augmented by adding five permutations of the principal stress and strain components in order to obtain a database that accounts for the isotropy, but no concept regarding an extension towards anisotropy was given. In Reference 29 an approach for the correction of finite hyperelastic models was presented and then showcased in interesting biomechanical applications in Reference 30, but again limited to isotropic material behavior. Molecular dynamics simulations of polymers have been used in Reference 31 in order to generate data and train a feed-forward neural network (FFNN) as a constitutive model in the context of isotropic finite hyperelasticity. Starting from a small strain highly nonlinear model, the radial numerically explicit potentials were suggested in Reference 32 as an extension of the NEXP proposed first in Reference 33 which employs a tensor decomposition into amplitude and direction followed by kernel interpolation. The method was later refined, compare References 34,35, and combined with ROM for the creation of efficient surrogate models for finite strain hyperelasticity in two- and three-scale simulations. In Reference 36, microstructural

simulations have been conducted to generate data for the calibration of a FFNN identifying the constitutive behavior of nonlinear elastic structures at finite strains, but without consideration of material symmetries. Incorporation of structural information can be enabled through, for example, geometric learning as in Reference 37, where polycrystals were represented by graphs and processed through graph convolution networks extracting relevant features for subsequent networks predicting the hyperelastic material behavior. A recent approach developed in Reference 38 demonstrates how machine learning models for anisotropic finite hyperelasticity can be constructed at minimal intrusion. The approach shows good flexibility and accurate predictions for lattice structures with pronounced nonlinear behavior due to beam buckling. In the context of a data-driven design optimization and manufacturing process for nonlinear metamaterials,³⁹ demonstrated parametrized constitutive formulations based on radial basis functions. Recently, Reference 40 included pattern information into a neural network-based, nonlinear elastoplastic model in order to characterize and design 2D network-like cellular metamaterials.

The present work extends the machine learning approach of Reference 38. Hereby, it is assumed that a solely state-dependent material model is able to capture the main constitutive response of lattice metamaterials showing instabilities. The present approach develops an anisotropic hyperelastic material model with parametric dependency for the representation and optimization of metamaterials with respect to the cell material and topology. For this aim, parametric unit cells of the considered anisotropic beam lattice metamaterials are simulated with periodic boundary conditions using a finite strain framework, exhibiting highly nonlinear behaviors due to instabilities. Hereby, the cell topology and the material properties of the elastic beams are varied in order to identify the quantities and properties relevant for a potential constitutive model. Then, the machine learning approach of Reference 38 is extended by including the parametric dependency in the artificial neural network (ANN) formulation. This elegant and flexible, non-intrusive extension is considered as a key property of the approach taken here, since material and, especially, topological dependency of material behavior is non-trivial in its incorporation in constitutive models. For the training of the model, a universal sample weighting strategy is developed such that the calibrated machine learning model approximates equally well the material response for stiff and compliant structures and independently of the loading scenario. The authors offer open access to the calibration data through the GitHub repository <https://github.com/CPSHub/sim-data>. Finally, the calibrated parametric material model is used for the optimization of unit cell material and topology in two examples, showcasing its potential applications for prescribed deformation and stress data, even in the case of incomplete data. In summary, the novelties of the present work are:

- the simulation-based investigation of parametric lattice unit cells subject to large deformations and instabilities, and the analysis of the influence of material and topology parameters in tension and compression regimes,
- the formulation of a generally applicable model for anisotropic hyperelasticity by extending the work of Reference 38 in a non-intrusive form for arbitrary-dimensional parametric dependency,
- the design of a sample weighting strategy for calibration data in order to obtain a uniform model prediction quality across topology variation and corresponding magnitude of material response, and
- the applicability of the calibrated model for the optimization of topology and material for prescribed material behavior with complete and incomplete data.

The outline of the manuscript is as follows: In Section 2 the microstructural modeling of the lattice cells and their behavior with respect to topology and material parameters is outlined. In Section 3 the parametric hyperelastic material model based on ANNs is formulated, its training using a dedicated sample weighting strategy is described and its prediction quality for various loading cases is demonstrated. The application of the calibrated model for microstructural optimization with respect to cell material and topology is illustrated in Section 4 through two examples. The article concludes in Section 5 with a summary and remarks.

1.1 | Notation

A direct tensor notation is preferred throughout this work. Scalars (zeroth-order tensors) are denoted by italic characters, for example, a , b , W . First-order tensors are represented by lower case Latin characters, for example, \mathbf{a} , \mathbf{b} , at what an orthonormal basis $\{\mathbf{e}_1, \mathbf{e}_2, \mathbf{e}_3\}$ of the three-dimensional physical space is used for the representation of all tensors. Second-order tensors are denoted by upper case Latin characters, for example, \mathbf{A} , \mathbf{B} . The tensor product is denoted as \otimes .

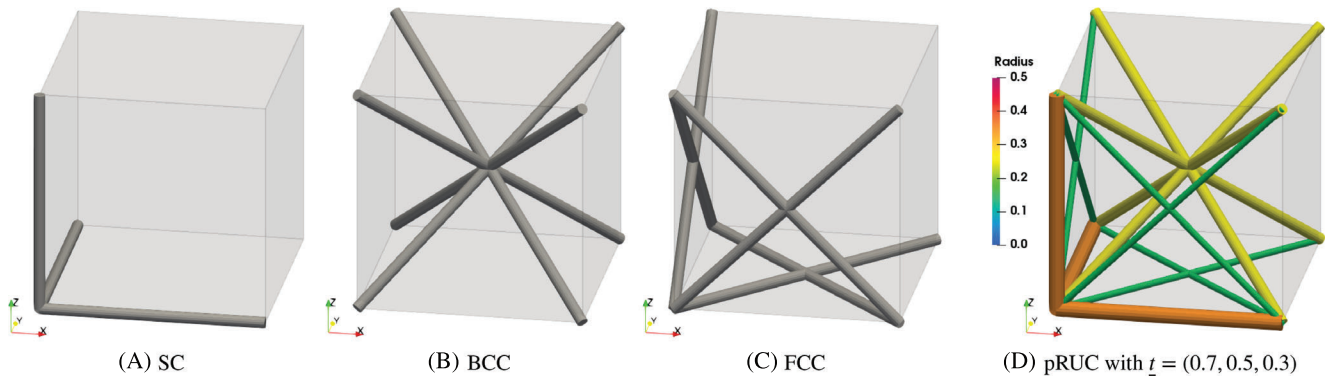


FIGURE 1 Simple cubic (SC), body-centered cubic (BCC), and face-centered cubic (FCC) basic lattice RUCs and example of a parametric unit cell (pRUC) with topology parameter vector $\underline{t} = (0.7, 0.5, 0.3)$

The composition of two second-order tensors is denoted as $\mathbf{AB} = \sum_{i,j,k=1}^3 A_{ik} B_{kj} \mathbf{e}_i \otimes \mathbf{e}_j$. The transpose of a second-order tensor is denoted by \mathbf{A}^T . The Frobenius norm of a second-order tensor is denoted as $\|\mathbf{A}\| = (\sum_{i,j=1}^3 A_{ij}^2)^{1/2}$. Vectors not connected to the physical basis are simply denoted as underlined characters, for example, \underline{a} , \underline{b} . The notation of physical quantities is leaned on standard continuum mechanics, that is, W is used for the elastic energy density, \mathbf{F} for the deformation gradient, and \mathbf{P} for the first Piola–Kirchhoff stress tensor.

2 | MICROSTRUCTURAL MODELING AND SIMULATION

2.1 | Parametric beam-lattice metamaterials

The present investigation considers beam-lattices with periodic microstructure as a representative of compliant, elastically deformable metamaterials. The repeated unit cell (RUC) of this class of metamaterials is composed of beams and is taken into account for the identification of the effective material behavior. Each beam in the RUC is assumed to be compliant with elastic material behavior under large deformations, meaning that the effective material behavior of the RUC is hyperelastic, that is, an effective elastic energy density W exists. Here, only metamaterials with cubic symmetry are considered and, without loss of generality, the RUCs are chosen as cubic with an edge length of $L = 10$ mm. The beams have circular cross-sections with a maximum radius of $r = 0.5$ mm, that is, a maximum aspect ratio of $a = 2r/L = 0.1$, which justifies the use of beam theories for microstructural modeling.

In the present work, a parametric RUC (pRUC) is considered in the sense that material and topology/morphology influences are taken into consideration. In terms of material, all beams in the RUC are assumed to have the same isotropic material properties, that is, Young's modulus E and Poisson's ratio ν , which will be considered in the effective material law. In terms of topology, three types of lattice structures are considered: simple cubic (SC), body-centered cubic (BCC), and face-centered cubic (FCC) cells, see Figure 1A–C.

The topology and morphology of a parametric RUC is represented by the parameter vector $\underline{t} = (t_1, t_2, t_3) \in \mathcal{T} = [0, 1]^3 \setminus [0, 0.2]^3$. The exclusion of a combination of very small topology parameters from \mathcal{T} is owing to aspects such as manufacturability and too soft overall response. The union of these three basic lattice types is formed with each component of $\underline{t} \in \mathcal{T}$ scaling the beam radius of the respective basic RUC (starting from 0.5 mm), t_1 representing the SC, t_2 the BCC, and t_3 the FCC cell contribution to the pRUC. As an example, consider $\underline{t} = (0.7, 0.5, 0.3)$, as depicted in Figure 1D. In this illustrated pRUC, the radii of the beams in the SC, BCC, and FCC cells are 0.35 mm ($= 0.7 \cdot 0.5$ mm, orange), 0.25 mm ($= 0.5 \cdot 0.5$ mm, yellow), and 0.15 mm ($= 0.3 \cdot 0.5$ mm, green), respectively.

In conclusion, the pRUC focused on within this work is hyperelastic, subjected to finite deformations and it can be influenced by a total of 5 scalar parameters: E , ν , and $\underline{t} = (t_1, t_2, t_3) \in \mathcal{T}$. These parameters will be addressed by the parameter vector \underline{p} as follows

$$\underline{p} = (E, \nu, t_1, t_2, t_3). \quad (1)$$

The effective behavior of such a microstructure is represented by an effective potential (referring to the effective elastic energy density) as

$$W = W(\mathbf{F}, \underline{p}), \quad (2)$$

where \mathbf{F} denotes the effective deformation gradient of the pRUC and \underline{p} describes the parametric dependency. Consequently, the effective stresses are given in terms of the corresponding first Piola–Kirchhoff stress as

$$\mathbf{P}(\mathbf{F}, \underline{p}) = \frac{\partial W}{\partial \mathbf{F}}(\mathbf{F}, \underline{p}). \quad (3)$$

2.2 | Numerical homogenization of beam-lattices

For the evaluation of the effective behavior of a pRUC, microstructural simulations with periodic displacement fluctuation boundary conditions are to be conducted in order to numerically quantify, that is, homogenize, the relation between \mathbf{F} , W , and \mathbf{P} for selected parameters \underline{p} .

For this purpose, the beam-lattices are mechanically modeled as geometrically exact, shear-deformable 3D beams and numerically simulated using an isogeometric collocation method, see Reference 41 for details. This beam model is geometrically nonlinear and, thus, it considers large deformations and rotations of the cross-sections, but employs a linear elastic, isotropic constitutive model with parameters E, ν , which limits the use to moderate strains. Furthermore, a rigid coupling of the beams is enforced at joints. For lattices with moderate aspect ratios, joint stiffening or weakening approaches may be necessary to achieve a good agreement of the model and physical experiments with (additively manufactured) lattice structures, see References 16,42. However, such approaches are not covered in this work, since the numerical methods presented are not tied to any specific materials and manufacturing technologies, and only aspect ratios $a \leq 0.1$ are considered.

For the homogenization of the metamaterial, effective deformation gradients \mathbf{F} are prescribed on the pRUC in the form of periodic displacement boundary conditions. Thus, for two beam centerline end-points or joint nodes $\mathbf{x}_1, \mathbf{x}_2$ located on opposite boundaries of the pRUC, periodic centerline displacements $\mathbf{u}_1, \mathbf{u}_2$ and consistent cross-section rotations $\mathbf{R}_1, \mathbf{R}_2$ are constrained by

$$\mathbf{u}_2 - \mathbf{u}_1 = \mathbf{F}(\mathbf{x}_2 - \mathbf{x}_1), \quad \mathbf{R}_2 = \mathbf{R}_1. \quad (4)$$

From the computed deformed configuration for prescribed \mathbf{F} , the potential energy $W(\mathbf{F})$ can be directly evaluated from the beam model. Furthermore, the effective first Piola–Kirchhoff stress tensor $\mathbf{P}(\mathbf{F})$ is computed in a column-wise fashion as

$$\mathbf{P}\mathbf{e}_i = \sum_{j=1}^3 P_{ji}\mathbf{e}_j = \frac{1}{L^2}\mathbf{f}_i, \quad i = 1, 2, 3, \quad (5)$$

where \mathbf{f}_i is the sum of all internal forces of the beams at the x_i -direction boundary of the pRUC and L is the edge length of the cuboidal pRUC ($L = 10$ mm in this work), compare Reference 19. Due to periodic rotations, bending moments vanish and do not contribute to the energy and stresses. It would also be possible to homogenize the resulting effective stress tangent tensors $\mathbb{C} = d\mathbf{P}/d\mathbf{F}$ from the beam model,¹⁹ however, this is not pursued here for various reasons, see also Section 3.3.2.

In the finite deformation regime, microstructures with slender struts, such as the beam-lattices considered here, can be subject to mechanical instabilities in the form of buckling and snapping of the struts. In numerical simulations, these instabilities occur in the form of diverging incremental nonlinear solution processes once a critical load level is reached. Since, in practice, the onset of buckling is impacted by—for example, manufacturing-related—imperfections, nonlinear post-buckling analyses are often performed using perturbation approaches, see, for example, References 43–45. That is, first a linear buckling analysis is carried out and then some of the eigenmodes are prescribed as perturbations on the beam centerlines for the nonlinear analysis, see for instance.¹⁶ However, this approach requires a lot of manual interference, such as selecting specific eigenmodes and choosing suitable scaling factors. Here, we use a simple stochastic approach

based on random geometric perturbations of the centerline. For this purpose, the initially straight centerlines of the beams are represented as B-Spline curves of degree 4 and their 5 control points are randomly perturbed within the cross-section plane. The amplitude of the perturbation is chosen as normally distributed with a mean of 0 and a variance of $0.01L$, and the direction of the perturbation is assumed to be uniformly distributed in the cross-section plane. In principle, for given \underline{t} and based on the results of multiple random instances, the corresponding average values of the effective potential W and effective stresses \mathbf{P} could be computed. However, as it will be demonstrated in Section 2.3, the simple lattice perturbation approach yields negligible deviations and sufficient accuracy and reliability for the characterization of the effective cell behavior already using a single random instance.

2.3 | Influence of perturbations and lattice parameters

In order to simulate the effective behaviors of the pRUC also in the post-buckling regime, the stochastic perturbation approach is employed. Since simulating a large number of random instances for each given pRUC (see Section 3.3.1) to average the W and \mathbf{P} would be computationally very expensive, the question arises, how much variation is actually encountered by different random instances of the same cell compared to the variation between different values of the topological parameters $\underline{t} \in \mathcal{T}$.

To investigate this in a clear and simple example, $t_1 = 0$ (SC cell) and $t_2 = 1$ (BCC cell) are kept constant and only $t_3 \in \{0.8, 0.9, 1.0\}$ (FCC cell) is varied. The cells for the corresponding parameter $\underline{t} \in \{(0.0, 1.0, 0.8), (0.0, 1.0, 0.9), (0.0, 1.0, 1.0)\}$ are illustrated in Figure 2 from left to right.

The values for \mathbf{F} , W , and \mathbf{P} for the selected cells are depicted in Figure 3. The plot range for the potential and stress values is kept constant over the rows in Figure 3 in order to visualize the impact of t_3 on $W \in [0, 250]$ J/m³ and $P_{ij} \in [-400, 1200]$ Pa. For each \underline{t} ten random instances were simulated, the material parameters of the beams being $E = 1$ MPa and $\nu = 0.45$. The boundary conditions are implemented such that all off-diagonal deformation components are set to zero but F_{12} . The deformation components F_{11} and F_{12} are prescribed through linear functions, (see, blue and orange lines in Figure 3), F_{22} and F_{33} are free, and $P_{33} = P_{22} = 0$ is imposed. The results are displayed in Figure 3 over F_{11} . This simulation case is interesting from the point of view that structural instabilities are triggered in both tensile ($F_{11} > 1$) and compressive ($F_{11} < 1$) regimes, as it can be seen by the abrupt change of stress tangents, in particular for the P_{12} and P_{21} stress components. From this point on, potential and stress values will be addressed and illustrated in all figures in Joule per cubic meter (J/m³) and Pascal (Pa), respectively. Only values for E will be addressed in megapascal (MPa) due to their standard order of magnitudes for various materials relevant in additive manufacturing of soft, flexible metamaterials.

In the first column of Figure 3 all nine components of \mathbf{F} for all ten instances of each \underline{t} are depicted and colored as indicated by the legend. The second and third columns show the corresponding potential values W and all nine components of \mathbf{P} , respectively. The first row shows the ten instances for $\underline{t} = (0.0, 1.0, 0.8)$, the second one for $\underline{t} = (0.0, 1.0, 0.9)$, and the third one for $\underline{t} = (0.0, 1.0, 1.0)$. These results show that the specific random instances only exhibit minor quantitative differences and in all cases closely reflect the highly nonlinear qualitative effective behavior. Further, the quantitative influence (in terms of energy and stress amplitudes) and the qualitative influence (in terms of buckling points and stress paths) of the topology parameters on the constitutive behavior is clearly visible in Figure 3, even though only t_3 is slightly

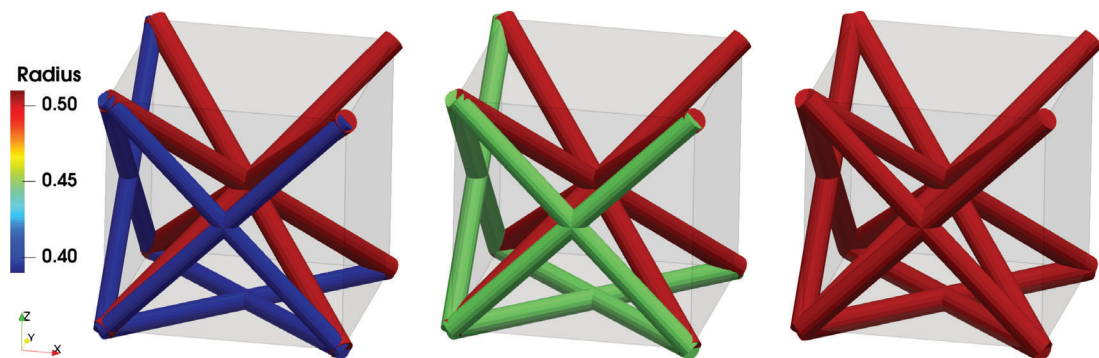


FIGURE 2 Considered cells for: $\underline{t} = (0.0, 1.0, 0.8)$ (left), $\underline{t} = (0.0, 1.0, 0.9)$ (middle), and $\underline{t} = (0.0, 1.0, 1.0)$ (right)

varied. For instance, for $t_3 = 0.8$ (top row in Figure 3) the potential and stress values are much lower than for $t_3 = 1.0$ (bottom row in Figure 3), visible due to the common plot ranges of all rows. Further, for $t_3 = 1.0$ the qualitative behavior of P_{11} clearly changes since in the compression regime ($F_{11} < 1$) it crosses the path of the P_{12} in *all* ten instances. This is not the case for $t_3 = 0.8$, where P_{11} stays above the P_{12} path in all ten instances. This simple example already indicates that changes in \underline{t} do not only affect the magnitude of corresponding 3-dimensional stresses at the onset of the structure instability, but also their qualitative behavior.

Furthermore, these results suggest that the variation between random instances may be considered negligible in practical situations. This observation is in agreement with the findings of Reference 16, where buckling eigenmodes were applied for post-buckling analysis. There, a minor influence of the perturbation factors could be observed, too, and the results were validated against experiments with PolyJet 3D printed lattices, which showed a very reproducible behavior. Thus, instead of computing and averaging several instances, or training a constitutive model on all instances for a single \underline{t} , we only use a single randomly perturbed instance for quantifying the effective behavior of each pRUC. This greatly reduces the computational effort and the amount of calibration data for the material models to be developed in Section 3.

For further illustration of the influence of the topology parameters \underline{t} , in Figure 4, a relatively soft structure with $\underline{t} = (0.125, 0.345, 0.255)$ (top) and a stiff one with $\underline{t} = (0.995, 0.885, 0.975)$ (bottom) are considered. It can be clearly seen that the topology parameters drastically affect the effective behavior of the pRUC in terms of the absolute magnitudes and qualitative properties, in particular with respect to the stress values. Between the stiff and the soft illustrated cells, roughly a factor of $\approx 4000/80 = 50$ between the maximum absolute P_{11} stress values is encountered. If, for instance, the maximum absolute stress value in compression ($F_{11} < 1$) of the compliant structure (top row in Figure 4) and the maximum stress

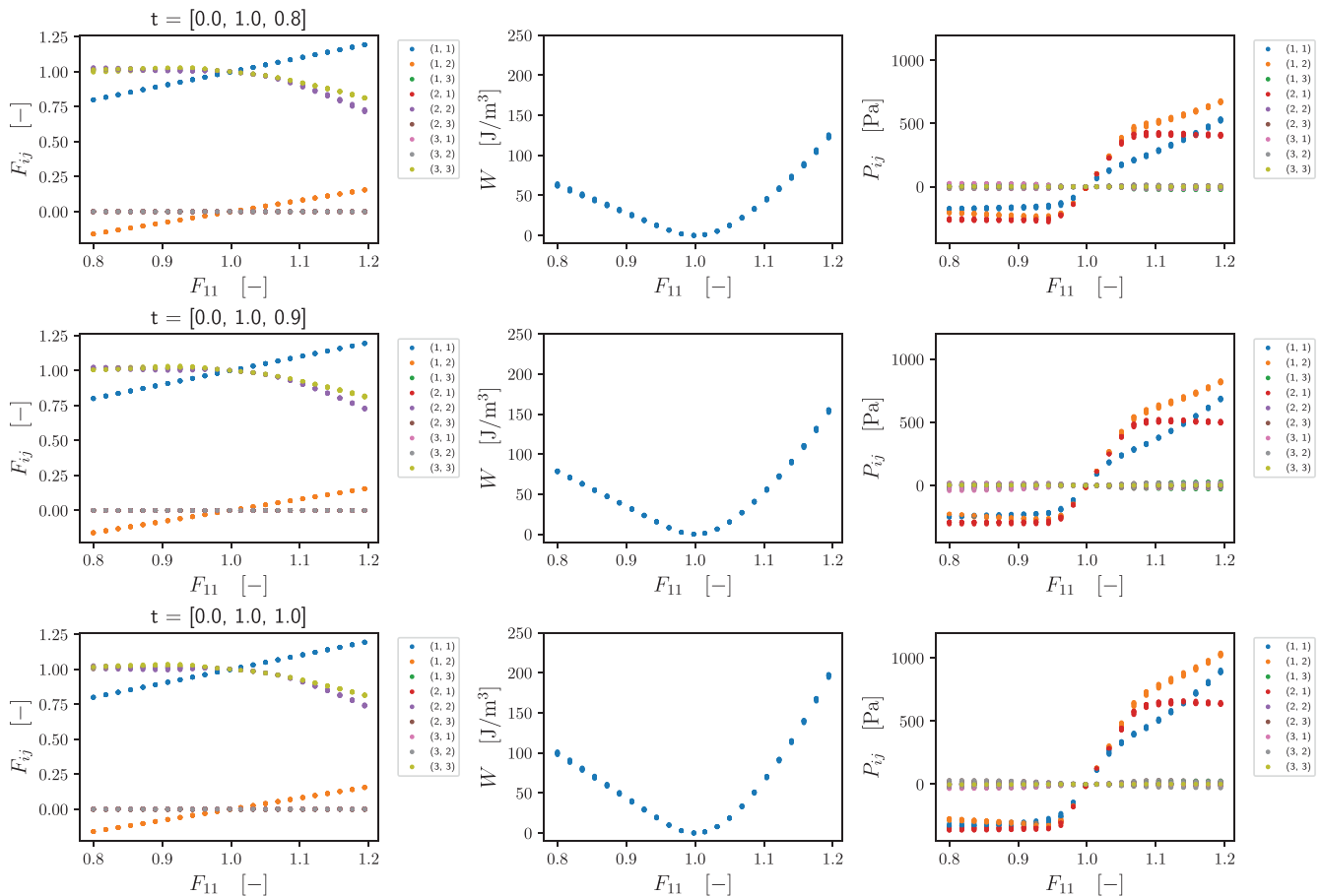


FIGURE 3 Effective behavior of ten instances for three topology parameters: first row $\underline{t} = (0.0, 1.0, 0.8)$, second row $\underline{t} = (0.0, 1.0, 0.9)$, and third row $\underline{t} = (0.0, 1.0, 1.0)$. The first column illustrates all nine components of \mathbf{F} of all ten instances, the second and third columns represent W (in J/m^3) and all nine components of \mathbf{P} (in Pa), accordingly

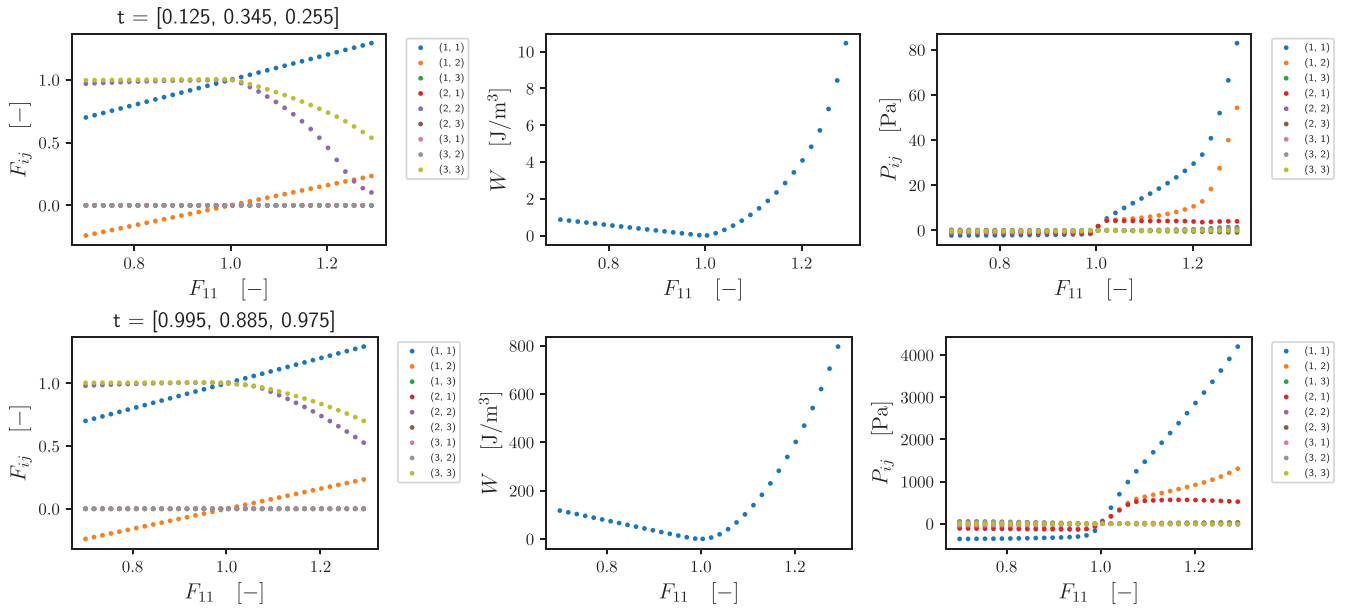


FIGURE 4 Effective behavior of a single instance for two topology parameters: first row compliant cell behavior with $\underline{t} = (0.125, 0.345, 0.255)$, and second row stiff cell behavior with $\underline{t} = (0.995, 0.885, 0.975)$. The first column illustrates all 9 components of \mathbf{F} , the second and third columns represent W (in J/m^3) and all 9 components of \mathbf{P} (in Pa), accordingly

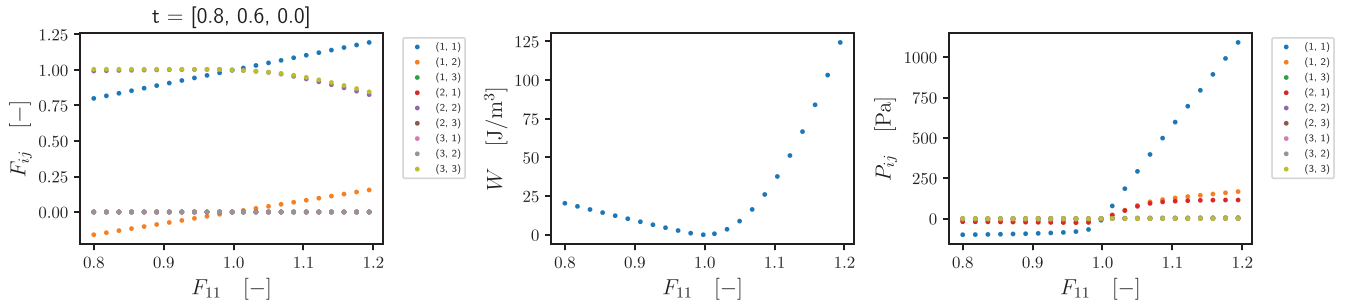


FIGURE 5 Components of \mathbf{F} , effective potential W (in J/m^3) and components of \mathbf{P} (in Pa) for a single instance with $\underline{t} = (0.8, 0.6, 0.0)$, $E = 10^6$ Pa = 1 MPa and $\nu = 0.45$

value in tension ($F_{11} > 1$) of the stiff structure (bottom row in Figure 4) are compared, then a relative deviation over several orders of magnitude is immediately obvious. These large changes in the qualitative and quantitative stress response depend on the topology parameters and the loading case of the cell. Capturing these effects in a compact substitute model for the parametric metamaterials is considered the most challenging task in the present work.

2.4 | Influence of material parameters

In addition to the topology parameters $\underline{t} \in \mathcal{T}$, also the isotropic material parameters of the beams E, ν influence the effective behavior of the pRUC. To investigate their qualitative influence, a fixed topology $\underline{t} = (0.8, 0.6, 0.0)$ and variable linear elastic material parameters for the beams are considered: $E \in [0.1, 10]$ MPa and $\nu \in (-1, 0.5]$. The boundary conditions stated in Section 2.3 are implemented. All nine components of \mathbf{F} and \mathbf{P} of a specific random instance for $E = 1$ MPa and $\nu = 0.45$ are depicted in Figure 5. Again, it can be seen that instabilities may occur in both tension ($F_{11} > 1$) and compression ($F_{11} < 1$).

First, we are interested in the influence of the Young's modulus E . For $E \in \{0.1, 1, 10\}$ MPa and fixed $\nu = 0.45$, the effective behavior of the pRUC is simulated using four random instances per E -value. In Figure 6, the potential W and

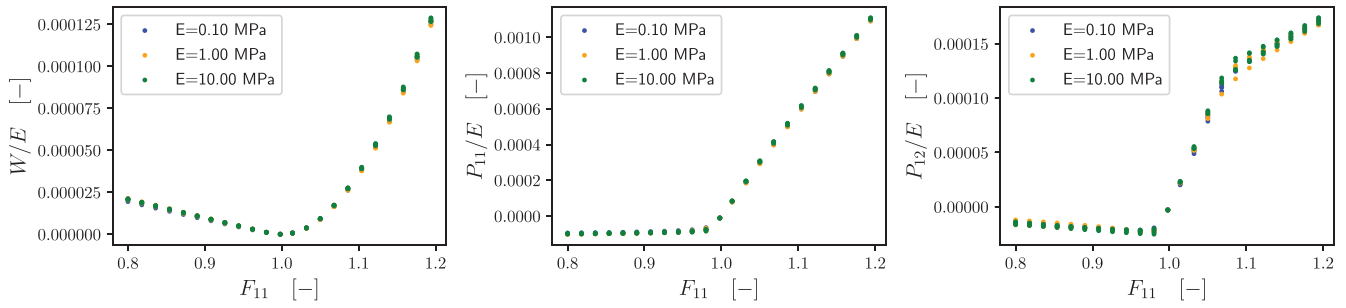


FIGURE 6 Variation of E : Effective potential W (in J/m^3) and stress components P_{11} and P_{12} normalized by E for $\underline{t} = (0.8, 0.6, 0.0)$, $\nu = 0.45$ and $E \in \{0.1, 1, 10\}$ MPa (four instances per E -value)

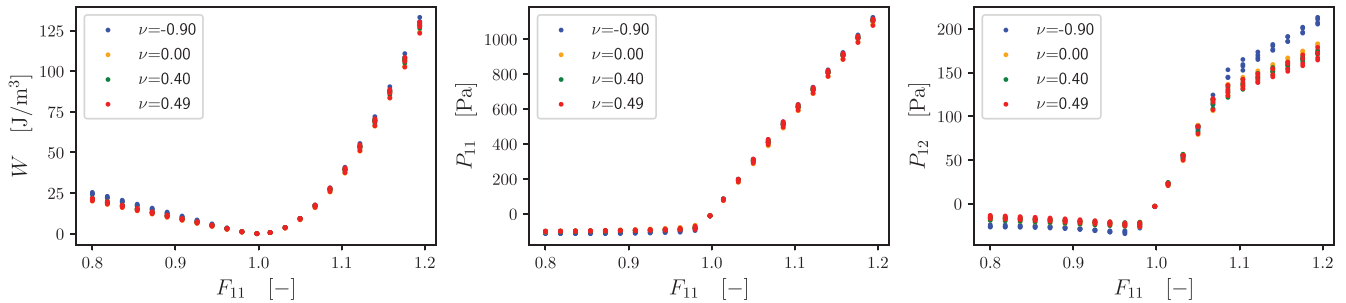


FIGURE 7 Variation of ν : Effective potential W (in J/m^3) and stress components P_{11} and P_{12} (in Pa) for $\underline{t} = (0.8, 0.6, 0.0)$, $E = 1$ MPa and $\nu \in \{-0.9, 0.0, 0.4, 0.49\}$ (four instances per ν value)

the stress components P_{11} and P_{12} , all normalized by E , are depicted for all twelve simulations, that is, four instances for each of the three E -values. It can be clearly seen, that—ignoring the negligible influence of the random instances—a master curve exists. This means that the constitutive behavior of the pRUC is linear in E . This is expected, since the linear elastic constitutive model of the beams is linear in E and all beams in the pRUC have the same E and, therefore, rescaling E simply rescales the potential and stress values. Moreover, this hints at an instability behavior of the pRUC dominated by geometric and not constitutive effects. Note that, so far, these observations are limited to the present load case and to $\nu = 0.45$.

Now, the influence of ν is to be examined. With fixed $E = 1$ MPa and varying $\nu \in \{-0.9, 0.0, 0.4, 0.49\}$, the effective behavior of the pRUC is simulated for four random instances per ν -value. The results are illustrated in Figure 7, showing 16 simulations in each plot, that is, four instances for each of the four ν -values. It can be seen that for $\nu \geq 0$ almost all curves can be described by one master curve. For $\nu = -0.9$, the beams have a dominant bending behavior due to large shear modulus values $G = E/(2(1 + \nu)) = 5E$. This seems to affect a part of the effective behavior in buckling, compare the blue curves for P_{12} in Figure 7. However, engineering base materials such as polymers and metals have positive Poisson’s ratios, while auxetic materials are typically also metamaterials and thus impractical for use as constituents of a microstructure.

Based on the observations in this section, it can be concluded that a single pair of chosen $E_0 > 0$ and $\nu_0 > 0$ suffices for practical cases, since E enters linearly in the constitutive behavior and for materials with $\nu \geq 0$ the deviations appear to be negligible. Material models calibrated on simulation data based on chosen E_0 and ν_0 can then be rescaled for new E and may be of pragmatic use for materials with different ν .

3 | CONSTITUTIVE MODELING FOR PARAMETRIC METAMATERIALS

Having introduced the pRUCs of cubic beam-lattices as a specific example for a parametric metamaterial along with their numerical modeling at finite deformations, a parametric anisotropic hyperelastic constitutive model is to be formulated such that it can represent their highly nonlinear effective behavior.

3.1 | Basic theory of anisotropic hyperelasticity

The potential of an anisotropic hyperelastic material under finite deformations with parametric dependency is addressed by the function $W(\mathbf{F}, \underline{p})$ as defined in (2), where $\mathbf{F} \in \text{Inv}^+$ and $\underline{p} \in P \subset \mathbb{R}^{d_p}$ denote the deformation gradient and the parameter vector, respectively. The set of invertible tensors with positive determinant is denoted by Inv^+ , while P represents the set of admissible parameters, which will be specified later on. The dimension of the parameter variable is addressed by d_p .

In order to fulfill the principle of objectivity, see, for example, Reference 46, the potential W is expressed through a function \hat{W} in terms of the right Cauchy-Green tensor $\mathbf{C} = \mathbf{F}^T \mathbf{F}$ and the parameters \underline{p} according to:

$$W(\mathbf{F}, \underline{p}) = \hat{W}(\mathbf{C}, \underline{p}). \quad (6)$$

The material symmetry group is described by the collection G of symmetry transformations \mathbf{Q}_i ($i = 1, 2, \dots$)

$$G = \{\mathbf{Q}_1, \dots\} \subset \text{SO}(3), \quad (7)$$

forming a subgroup of the manifold of proper rotations $\text{SO}(3)$ and fulfilling, see, for example, Reference 47,

$$W(\mathbf{F}, \underline{p}) = W(\mathbf{F}\mathbf{Q}, \underline{p}) \quad \forall \mathbf{Q} \in G, \mathbf{F} \in \text{Inv}^+, \underline{p} \in P. \quad (8)$$

For instance, the material symmetry of a cubic hyperelastic material is then described by the Schönflies octahedral group O_h with 24 rotations, see, for example, Reference 48. Note that the symmetry transformations $\mathbf{Q} \in G$ do not affect the parameter vector \underline{p} of the present work: the material parameters are invariant under symmetry transformations and \underline{t} comprises topological parameters which, by definition, are invariant with respect to affine transformations.

The second Piola–Kirchhoff stress tensor \mathbf{S} is related to \mathbf{P} and to \hat{W} compare (6) as follows

$$\mathbf{P} = \mathbf{F}\mathbf{S}, \quad \mathbf{S} = 2 \frac{\partial \hat{W}}{\partial \mathbf{C}}. \quad (9)$$

The above relation is gained from application of the chain rule to the hyperelastic relation (3). The material symmetry conditions for the first Piola–Kirchhoff stress are, see, for example, Reference 49,

$$\mathbf{P}(\mathbf{F}, \underline{p}) = \mathbf{P}(\mathbf{F}\mathbf{Q}, \underline{p})\mathbf{Q}^T \quad \forall \mathbf{Q} \in G, \mathbf{F} \in \text{Inv}^+, \underline{p} \in P. \quad (10)$$

Note that (10) is automatically induced by W fulfilling (8) and that the presented framework is applicable to extended parameter dependency as long as the material symmetry transformations do not affect the considered \underline{p} .

3.2 | Parametric material modeling based on machine learning

To formulate a parametric anisotropic hyperelastic constitutive model, the present work extends one of the machine learning (ML) approaches recently introduced in Reference 38. More specifically, the ML potential approach with group symmetrization is considered in this work due to its excellent properties in fitting the constitutive behavior of beam-lattices with highly nonlinear behaviors triggered by instabilities induced by buckling on the level of the struts. This ML potential approach is now extended to include a parametric dependency \underline{p} , namely on the material parameter E and the topological parameters \underline{t} .

Following,³⁸ we first consider a ML core model $\tilde{W}^{\text{ML}}(\mathbf{C}, \underline{p})$, which depends on a total of $6 + d_p$ scalar inputs (six degrees of freedom of \mathbf{C} and d_p parameters in \underline{p}). The ML core model \tilde{W}^{ML} can be, in principle, any twice continuously differentiable function with respect to \mathbf{C} . We then perform a group symmetrization as follows

$$\hat{W}^{\text{ML}}(\mathbf{C}, \underline{p}) = \frac{1}{\#(G)} \sum_{\mathbf{Q} \in G} \tilde{W}^{\text{ML}}(\mathbf{Q}^T \mathbf{C} \mathbf{Q}, \underline{p}). \quad (11)$$

The potential of the parametric ML-potential approach is then defined through

$$W^{\text{ML}}(\mathbf{F}, \underline{p}) = \hat{W}^{\text{ML}}(\mathbf{C}, \underline{p}). \quad (12)$$

The group symmetrization (11), originally introduced in Reference 38 in terms of \mathbf{F} , ensures that the final potential (12) fulfills all material symmetry group conditions (8) by construction, that is, independent of any further parametric extension of the core model \tilde{W}^{ML} . This approach offers a non-intrusive and highly flexible ansatz for any given (finite-dimensional) anisotropy group G . Furthermore, the incorporation of the parametric dependency through extension of the approach of Reference 38 is as straight-forward as humanly possible through a simple increase of number of inputs in the underlying machine learning approach. The simplicity of this approach makes it not only non-intrusive but highly adaptable to even higher-dimensional parametric dependencies, as long as these are not affected by symmetry transformations.

Compared to alternative approaches relying on the usage of structural tensors and invariants of groups, see, for example, Reference 27, the present approach does not require the search and definition of a specific set of invariants. For instance, if cubic materials are of interest, invariants involving *at least* structural tensors of second- and fourth-order are necessary. Since the vast majority of material symmetry groups in material science are very well studied, the collection G is most probably available for a high number of practical cases, such that the approach of the present work is easily implementable.

As in Reference 38, the present approach considers ANNs for the ML core model \tilde{W}^{ML} . Since the constitutive behavior of the pRUC under investigation is solely state-dependent and not path-dependent, it suffices to use FFNNs for the core model. Based on the examinations of the pRUC in the previous section, the present work considers a dimensionless scaling parameter $E_s \in (0, \infty)$, that is, the Young's modulus of the beam material $E = E_s \cdot E_0$ for a yet to be chosen reference E_0 , and the topology parameters \underline{t} . The parameter vector \underline{p} is from this point on re-defined as

$$\underline{p} = (E_s, t_1, t_2, t_3) \in \mathbb{P} = (0, \infty) \times \mathcal{T} \quad (13)$$

with $\mathcal{T} = [0, 1]^3 \setminus [0, 0.2]^3$ and $d_p = 4$. The constant reference parameter $v_0 = 0.45$ is excluded from \underline{p} for simplicity. The core model for the present work is now formulated based on a FFNN taking in Green's strain tensor $\mathbf{E} = (\mathbf{C} - \mathbf{I})/2$ and the translated topology parameter $\underline{\tau} = \underline{t} - (0.5, 0.5, 0.5)$ as follows

$$\tilde{W}^{\text{ML}}(\mathbf{C}, \underline{p}) = E_s E_0 \text{FFNN}(\mathbf{E}, \underline{\tau}). \quad (14)$$

We consider the usage of \mathbf{E} and $\underline{\tau}$ in order to provide input features around the origin for better calibration of the networks. The dimensionless parameter dependency with E_s is explicitly used in order to rescale the output of the FFNN based on the observation of the previous section that the constitutive behavior is linear in Young's modulus E . More explicitly, the final model (12) can be calibrated with data based on a reference Young's modulus, for example, $E_0 = 5$ MPa, and later on evaluated for a different elastic modulus, for example, $E = 7.5$ MPa = $E_s E_0$, by simply using the appropriate dimensionless E_s for rescaling, for example, $E_s = 1.5$ in the current example. The parameter dependency $\underline{p} = (E_s, t_1, t_2, t_3)$ then provides the ability of the final model (12) to be of use for cell material and topological variations.

For the pRUC considered explicitly in this work, the material symmetry group G is the group for cubic objects. Thus, the cubic group with 24 rotation matrices is used. However, it should be emphasized that the non-intrusive approach (12) could be used for *any* given G , for example, for a finite subgroup of transversely isotropic materials in the context of pseudo-unidirectional fiber-reinforced hyperelastic materials.

The FFNNs considered in this work are composed of n_H hidden layers and a homogeneous number n_{NH} of neurons in each hidden layer. The network architecture is shortly denoted as $\mathcal{N}[n_H, n_{NH}]$. For instance, $\mathcal{N}[3, 128]$ refers to a FFNN with 3 hidden layers and 128 neurons per hidden layer. The layers are supposed to be fully connected throughout. In all hidden layers, the softplus function

$$s(x) = \log(1 + \exp(x)) \quad (15)$$

is used as activation function in order to ensure (infinite) differentiability of the model. In the output layer of the model, a single neuron and the identity activation function $\text{Id}(x) = x$ are used in order to get a scalar output out of the linear

combination of the functions of the last hidden layer. After fixing the architecture of the core model, the weights and biases of all layers must be calibrated. The collection of all weights and biases is referred to as $\underline{\omega} \in \mathbb{R}^{n_\omega}$. The total number of calibration parameters n_ω in the model (12) is given by

$$n_\omega = \sum_{l=1}^{n_H+1} (n_{l-1} + 1)n_l \quad \text{with} \quad n_0 = 9, \quad n_l = n_{NH} \quad (l = 1, \dots, n_H), \quad n_{n_H+1} = 1, \quad (16)$$

where $n_0 = 9$ denotes the number of network inputs (six degrees of freedom of \mathbf{E} and three shifted topology parameters $\underline{\tau}$) and $n_{n_H+1} = 1$ the scalar output in the output layer. For instance, the network $\mathcal{N}[3,128]$ has $n_\omega = 34,433$ calibration parameters. As mentioned above, the incorporation of the parametric dependency through a simple increase of the size of the input in the underlying FFNN is straight-forward in the present approach. This non-intrusive property is considered a major advantage compared to analytical mechanical models, for which the incorporation of complex topological dependencies is far from trivial.

Finally, it should be noted that the present approach based on a core FFNN with the softplus activation function is differentiable not only with respect to \mathbf{F} , but also with respect to \underline{p} . Implementations of this approach with modern ML libraries, for example, TensorFlow 2.4, can take advantage of automatic differentiation routines in order to obtain the corresponding gradients. This makes the computation of the stresses, stress tangents, and topological sensitivities trivial and computationally highly efficient on GPU-based systems, especially for a large number of inputs. In contrast to real experiments and structures simulations, where the extraction of gradient-based quantities as, for example, the effective stress tangent $\mathbb{C} = d\mathbf{P}/d\mathbf{F} = d^2W/d\mathbf{F}^2$ is technically involved (if possible at all), the presented differentiable FFNN-model offers clear computational advantages once calibrated.

3.3 | Training approach

3.3.1 | Data generation strategy

For the calibration of the parametric ML-potential model W^{ML} (12), or the training of the underlying FFNN model \tilde{W}^{ML} (14), respectively, data involving variations of the inputs, that is, \mathbf{F} and \underline{t} , and the corresponding system response, that is, W (and \mathbf{P}), are required. The dependency on E and E_s is trivial such that only calibration data for $E_0 = 1$ MPa will be generated and $E_s = 1$ will be fixed during model calibration, if not otherwise explicitly stated.

For the generation of calibration data involving \mathbf{F} , W , and \mathbf{P} , the present work relies on the homogenization of the pRUCs as described in Section 2.2. In the following, eight experimentally motivated mechanical scenarios partially prescribing some deformation and some stress components are considered. Hereby, a simulation process parameter $\lambda \in [-1, 1]$ is introduced such that all deformation and stress components depend at least implicitly on λ . This dependency is explicitly given for the components with prescribed linear dependency on λ , while omitted for the rest. The eight experimentally motivated scenarios are defined as follows:

Scenario 1 - uniaxial stress state:

$$\mathbf{F} = \begin{pmatrix} 1 + 0.3\lambda & 0 & 0 \\ 0 & F_{22} & 0 \\ 0 & 0 & F_{33} \end{pmatrix} \mathbf{e}_i \otimes \mathbf{e}_j, \quad P_{22} = P_{33} = 0. \quad (17)$$

Scenario 2 - biaxial deformation with ratio of 1 (axis 1 vs. 2)

$$\mathbf{F} = \begin{pmatrix} 1 + 0.3\lambda & 0 & 0 \\ 0 & 1 + 0.3\lambda & 0 \\ 0 & 0 & F_{33} \end{pmatrix} \mathbf{e}_i \otimes \mathbf{e}_j, \quad P_{33} = 0. \quad (18)$$

Scenario 3 - planar deformation

$$\mathbf{F} = \begin{pmatrix} 1 + 0.3\lambda & 0 & 0 \\ 0 & 1 & 0 \\ 0 & 0 & F_{33} \end{pmatrix} \mathbf{e}_i \otimes \mathbf{e}_j, \quad P_{33} = 0. \quad (19)$$

Scenario 4 - volumetric deformation

$$\mathbf{F} = \begin{pmatrix} 1 + 0.3\lambda & 0 & 0 \\ 0 & 1 + 0.3\lambda & 0 \\ 0 & 0 & 1 + 0.3\lambda \end{pmatrix} \mathbf{e}_i \otimes \mathbf{e}_j. \quad (20)$$

Scenario 5 - simple shear deformation

$$\mathbf{F} = \begin{pmatrix} 1 & 0.3\lambda & 0 \\ 0 & 1 & 0 \\ 0 & 0 & 1 \end{pmatrix} \mathbf{e}_i \otimes \mathbf{e}_j. \quad (21)$$

Scenario 6 - biaxial deformation with ratio of 2 (axis 1 vs. 2)

$$\mathbf{F} = \begin{pmatrix} 1 + 0.3\lambda & 0 & 0 \\ 0 & 1 + 0.15\lambda & 0 \\ 0 & 0 & F_{33} \end{pmatrix} \mathbf{e}_i \otimes \mathbf{e}_j, \quad P_{33} = 0. \quad (22)$$

Scenario 7 - biaxial deformation with ratio of 3 (axis 1 vs. 2)

$$\mathbf{F} = \begin{pmatrix} 1 + 0.3\lambda & 0 & 0 \\ 0 & 1 + 0.1\lambda & 0 \\ 0 & 0 & F_{33} \end{pmatrix} \mathbf{e}_i \otimes \mathbf{e}_j, \quad P_{33} = 0. \quad (23)$$

Scenario 8 - combined uniaxial and shear deformation

$$\mathbf{F} = \begin{pmatrix} 1 + 0.3\lambda & 0.24\lambda & 0 \\ 0 & F_{22} & 0 \\ 0 & 0 & F_{33} \end{pmatrix} \mathbf{e}_i \otimes \mathbf{e}_j, \quad P_{22} = P_{33} = 0. \quad (24)$$

These eight scenarios have also been considered in Reference 38 and provide mechanical scenarios mostly reproducible in experiments. The last mechanical scenario with prescribed paths for F_{11} and F_{12} was already applied in the previous Sections 2.3 and 2.4, since it shows that beam buckling and structural instabilities—reflected by abrupt changes of stress gradients—can be present in both compression *and* tension scenarios, compare Figure 4. For a given topology t_i , each of the mechanical scenarios is simulated for $\lambda \in [0, 1]$ (tension) and $\lambda \in [-1, 0]$ (compression) separately. This yields, strictly speaking, eight tension and eight compression cases, respectively. These will be referred to as the 16 simulation cases

$$\begin{aligned} C = \{ & \text{scenario 1 in tension } (\lambda \in [0, 1]), \text{ scenario 1 in compression } (\lambda \in [-1, 0]), \\ & \text{scenario 2 in tension } (\lambda \in [0, 1]), \text{ scenario 2 in compression } (\lambda \in [-1, 0]), \\ & \text{scenario 3 in tension } (\lambda \in [0, 1]), \text{ scenario 3 in compression } (\lambda \in [-1, 0]), \\ & \text{scenario 4 in tension } (\lambda \in [0, 1]), \text{ scenario 4 in compression } (\lambda \in [-1, 0]), \end{aligned}$$

scenario 5 in tension ($\lambda \in [0, 1]$), scenario 5 in compression ($\lambda \in [-1, 0]$),
 scenario 6 in tension ($\lambda \in [0, 1]$), scenario 6 in compression ($\lambda \in [-1, 0]$),
 scenario 7 in tension ($\lambda \in [0, 1]$), scenario 7 in compression ($\lambda \in [-1, 0]$),
 scenario 8 in tension ($\lambda \in [0, 1]$), scenario 8 in compression ($\lambda \in [-1, 0]$)} . (25)

For every topology \underline{t} and each of the $\#(C) = 16$ cases $c \in C$, a fixed number of $\#(S) = 151$ simulation steps (indexed by $s \in S$) with corresponding \mathbf{F} , \mathbf{W} and \mathbf{P} are recorded. Thus, for a single \underline{t} , $16 \cdot 151 = 2416$ data points are computed and the values of the strain energy density and the stresses are collected for the training of the ML model.

Sampling of the topology parameters $\underline{t} \in \mathcal{T}$ is conducted based on Latin hypercube sampling (LHS). In this work, 100 sampling points in the interior of the admissible domain \mathcal{T} are considered with LHS. In addition to these LHS samples, the edges and facets of the star-shaped domain are discretized manually, leading to an additional 158 points comprising also the seven admissible corners of the domain \mathcal{T} . Thereby it is guaranteed that all admissible parameter vectors can be obtained by convex combinations of training samples. The set $T \subset \mathcal{T}$ refers to these $\#(T) = 258$ topologies \underline{t} . It shall be noted that the solid volume fraction ranges from 0.0942% up to 14.5%, that is, the ratio between the volume fraction of these extremal pRUC is larger than 150, which illustrates the variety of the design space considered. Finally, the calibration dataset

$$D^C = \{(\mathbf{F}, \underline{t}, \mathbf{W}, \mathbf{P}) : (\mathbf{F}, \underline{t}, \mathbf{W}, \mathbf{P})_{[\underline{t}, c, s]}, \underline{t} \in T, c \in C, s \in S\} \quad (26)$$

contains then $\#(D^C) = \#(T) \cdot \#(C) \cdot \#(S) = 258 \cdot 16 \cdot 151 = 623,328$ data points with varying values for the inputs \mathbf{F} and \underline{t} and corresponding outputs \mathbf{W} and \mathbf{P} .

To confirm the accuracy of the machine learned model and its generalization capabilities for non-training queries, additional validation data is needed. In order to not grow the number of required samples too much, 20 topology parameter vectors maximizing the nearest neighbor distance to the set T are chosen. A similar approach was used successfully for ROM in the past.⁵⁰ The number of only 20 validation samples (each undergoing 16 loading cases at 151 steps) is justified by the previous non-parametric work,³⁸ where it was shown that the core of the hyperelastic model generalizes well for lattice metamaterials and is very well able to improve with growing datasets. The set of the 20 validation topology parameters is referred to as $V \subset \mathcal{T}$ and the resulting validation dataset D^V contains $\#(D^V) = \#(V) \cdot \#(C) \cdot \#(S) = 20 \cdot 16 \cdot 151 = 48,320$ data points for the inputs \mathbf{F} and \underline{t} and the corresponding outputs \mathbf{W} and \mathbf{P} .

These calibration and validation datasets are made openly accessible by the authors through the GitHub repository <https://github.com/CPSHub/sim-data>. The locations of all points from both datasets are visualized in Figure 8.

3.3.2 | Objective function and sample weighting

A standard objective function for the calibration of surrogate models is the mean squared error (MSE). In terms of the potential and stress data, we thus here consider the following two weighted error measures

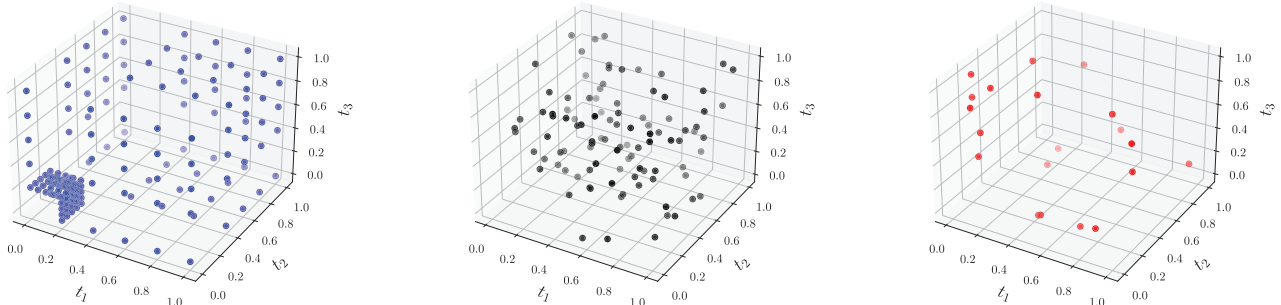


FIGURE 8 Sampled topologies: boundary points in blue (left), inner points in black from LHS (middle), and validation topologies in red (right)

$$wMSE^W = \frac{1}{\#(T)\#(C)\#(S)} \sum_{\underline{t} \in T} \sum_{c \in C} \sum_{s \in S} w_{[\underline{t},c,s]}^W (W_{[\underline{t},c,s]} - W_{[\underline{t},c,s]}^{ML})^2 \quad (27)$$

$$wMSE^P = \frac{1}{\#(T)\#(C)\#(S)} \sum_{\underline{t} \in T} \sum_{c \in C} \sum_{s \in S} w_{[\underline{t},c,s]}^P \frac{1}{9} \sum_{i_1=1}^3 \sum_{i_2=1}^3 ((\mathbf{P}_{[\underline{t},c,s]})_{i_1 i_2} - (\mathbf{P}_{[\underline{t},c,s]}^{ML})_{i_1 i_2})^2, \quad (28)$$

where the index $[\underline{t}, c, s]$ denotes the correspondence to the topology \underline{t} , case c and simulation step s , for example, $W_{[\underline{t},c,s]}^{ML} = W^{ML}(\mathbf{F}_{[\underline{t},c,s]}, (1, t_1, t_2, t_3))$. The weights $w_{[\underline{t},c,s]}^W$ for the potential error $wMSE^W$ and $w_{[\underline{t},c,s]}^P$ for the stress error $wMSE^P$ can be used to balance large differences in the output data and enhance the prediction quality of calibrated models. This is particularly important in the present work, since the potential and stress values of different structures can vary over several orders of magnitude, depending mainly on \underline{t} (which governs the solid material content inside of the pRUC) and on the applied load case c . Consider, for instance, Figure 4 again, illustrating the uniaxial-shear scenario for tension ($F_{11} > 1$) and compression ($F_{11} < 1$) for two substantially different topologies. Not only the maximum tension values of the stresses differ for these two topologies by a factor of around 50, but also the magnitudes of tension and compression cases vary significantly. This poses serious challenges for any material model required to yield accurate predictions, for example, for stiff structures (high values for the components of \underline{t}) in the tension case, as well as for compliant structures (low values in \underline{t}) in the compression case, for any of the 8 scenarios. A key driver for the pronounced dependency of the strain energy and the stresses on \underline{t} is due to the volume fraction of the solid: The cross-sections scale with t_i^2 and the length of the struts is constant.

In order to better quantify the constitutive behavior for a fixed topology \underline{t} and loading case c , we define the following l^2 -norms for the simulation sequences of the potential and stress values

$$\|W_{[\underline{t},c]}\|_{l^2} = \sqrt{\sum_{s \in S} W_{[\underline{t},c,s]}^2} \quad (29)$$

$$\|\mathbf{P}_{[\underline{t},c]}\|_{l^2} = \sqrt{\sum_{s \in S} \sum_{i_1=1}^3 \sum_{i_2=1}^3 (\mathbf{P}_{[\underline{t},c,s]})_{i_1 i_2}^2}. \quad (30)$$

Evaluation of the $\#(T)\#(C) = 1712$ l^2 -norms for all topologies and cases in the calibration dataset D^C is illustrated by their corresponding cumulative distribution functions in Figure 9 over a logarithmic scale. As shown in Figure 9, the l^2 -norms of the potential and stresses possess a wide range over five orders of magnitude, depending on the considered \underline{t} and c . This makes it very clear that a proper weighting strategy is required in the formulations of the MSEs in (27) and (28). Consequently, the present work introduces the following weights, which are formulated using the l^2 -norms for fixed topology \underline{t} and loading case c , and are thus independent of the step s :

$$w_{[\underline{t},c,s]}^W = \left(\frac{1}{\#(S)} \|W_{[\underline{t},c]}\|_{l^2}^2 \right)^{-1} \quad (31)$$

$$w_{[\underline{t},c,s]}^P = \left(\frac{1}{9\#(S)} \|\mathbf{P}_{[\underline{t},c]}\|_{l^2}^2 \right)^{-1}. \quad (32)$$

Inserting this particular choice of weights into (27) and (28), respectively, yields the weighted MSEs as relative errors

$$wMSE^W = \epsilon^W = \frac{1}{\#(T)\#(C)} \sum_{\underline{t} \in T} \sum_{c \in C} \epsilon_{[\underline{t},c]}^W, \quad \epsilon_{[\underline{t},c]}^W = \left(\frac{\|(W - W^{ML})_{[\underline{t},c]}\|_{l^2}}{\|W_{[\underline{t},c]}\|_{l^2}} \right)^2, \quad (33)$$

$$wMSE^P = \epsilon^P = \frac{1}{\#(T)\#(C)} \sum_{\underline{t} \in T} \sum_{c \in C} \epsilon_{[\underline{t},c]}^P, \quad \epsilon_{[\underline{t},c]}^P = \left(\frac{\|(\mathbf{P} - \mathbf{P}^{ML})_{[\underline{t},c]}\|_{l^2}}{\|\mathbf{P}_{[\underline{t},c]}\|_{l^2}} \right)^2, \quad (34)$$

using the squared norm over the load path defined by (29), (30). These relative error measures allow the quantification of relative model deviations from the expected behavior based on the most influential changes for the problem at hand, that is, topology and loading case. Naturally, values far below unity for $\epsilon^W \in [0, \infty)$ and $\epsilon^P \in [0, \infty)$ are expected for high quality models. In order to consider the errors of both the potential and stress data, the present work uses

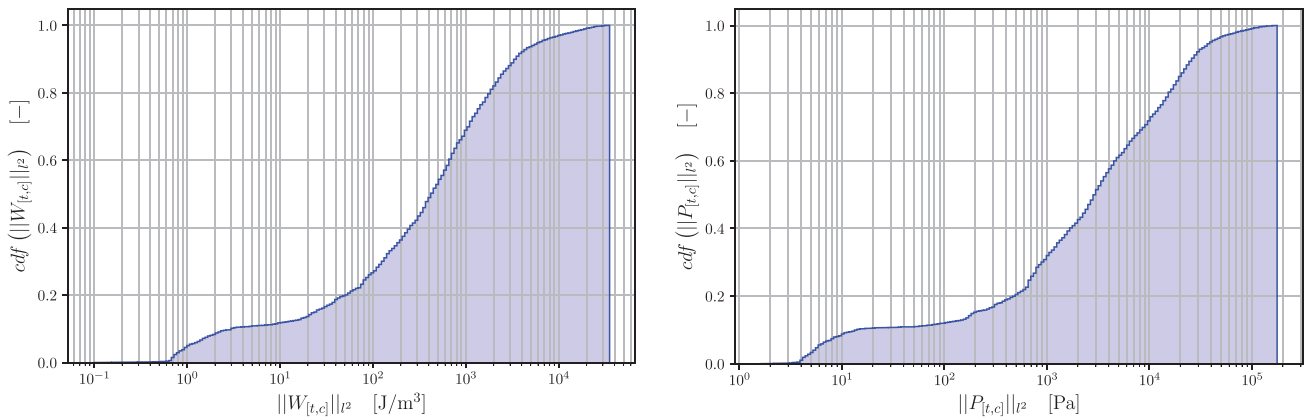


FIGURE 9 Cumulative distribution functions of the L^2 -norms $\|W_{[t,c]}\|_{L^2}$ (left) and $\|P_{[t,c]}\|_{L^2}$ (right)

$$\epsilon = \frac{1}{2} (\epsilon^W + \epsilon^P) = \frac{1}{\#(\mathbf{T})\#(\mathbf{C})} \sum_{\underline{t} \in \mathbf{T}} \sum_{c \in \mathbf{C}} \epsilon_{[\underline{t},c]}, \quad \epsilon_{[\underline{t},c]} = \frac{1}{2} (\epsilon_{[\underline{t},c]}^W + \epsilon_{[\underline{t},c]}^P) \quad (35)$$

as objective function for the calibration of the following ML models.

Above, the wMSEs and total error ϵ are formulated for the training dataset D^C , that is, for $\underline{t} \in \mathbf{T}$, but they can in the same fashion also be formulated for the validation dataset D^V , that is, for $\underline{t} \in \mathbf{V}$.

Besides potential and stress values, also the wMSE of the stress tangent tensor $\mathbb{C}(\mathbf{F}) = d^2W/d\mathbf{F}^2$ could be added to the objective function ϵ from (35), which might further improve accuracy or regularity of the calibrated models, compare Reference 37. However, this approach is not pursued here, because (i) the homogenization of \mathbb{C} from the beam model is rather elaborate,¹⁹ (ii) for other applications, \mathbb{C} might not be available from the microstructural simulations and is generally not available for experimental characterization data, and (iii) it would increase the computational effort for evaluating ϵ tremendously, since $d^2W^{ML}/d\mathbf{F}^2$ would have to be evaluated for each parameter $[\underline{t}, c, s]$ in each iteration of the optimization, including the symmetrization resulting from (11).

3.4 | Results

The machine learning-based parametric constitutive models introduced above have been implemented in Python 3.8.5 with TensorFlow 2.4 on a Windows system with a GeForce RTX 2080 Ti graphics card for GPU acceleration. The gradient of the ML models is obtained in TensorFlow 2.4 through automatic differentiation.

An architecture sweep is performed with the calibration dataset D^C and the validation dataset D^V . Different network architectures $\mathcal{N}[n_H, n_{NH}]$ with $n_H \in \{3, 4\}$ and $n_{NH} \in \{8, 16, 32, 64, 128\}$ are tested. Each architecture is initialized three times and trained for a maximum of 3000 epochs with a batch size of $2^{14} = 16,384$. Early stopping is used such that the model calibration is stopped if no improvement is achieved with respect to ϵ for the validation dataset D^V in a patience window of 500 epochs. The results for the objective function ϵ for the architecture sweep are tabulated in Table 1. The prediction qualities in terms of ϵ for D^V of the trained networks are shown in the middle column of Table 1 and range from 16% to 23% for $\mathcal{N}[3, 8]$ down to 4.7%–5% for $\mathcal{N}[4, 128]$. The analogous results for D^C in the right column are slightly better than for D^V , demonstrating that overfitting has been avoided and that the networks are able to generalize well. Of course, overfitting is mainly avoided through the early stopping of the trained networks and the use of training batches is also helping in avoiding pronounced overfitting.

For instance, the evolution of the objective ϵ for the largest and best performing model instance with $\mathcal{N}[4, 128]$ is illustrated in Figure 10. A maximum of 3000 epochs is allowed during training, but since ϵ for D^V is monitored and does not continue to improve over the patience window of 500 epochs, the training is stopped and the best performing state of the network with respect to D^V is restored, yielding $\epsilon = 0.0466$ for D^V and $\epsilon = 0.0367$ for D^C . This best performing instance of $\mathcal{N}[4, 128]$ is chosen for the rest of the section for an in depth examination. The chosen model is referred to from now on simply as \mathcal{M} . Naturally, as visible in Table 1, smaller networks achieve comparable quality. The present work simply

TABLE 1 Range of objective function ϵ for network architectures in initial sweep

Architecture	ϵ (validation)	ϵ (calibration)
$\mathcal{N}[3, 8]$	0.1564 ... 0.2345	0.1368 ... 0.1561
$\mathcal{N}[3, 16]$	0.0615 ... 0.0742	0.0542 ... 0.0690
$\mathcal{N}[3, 32]$	0.0558 ... 0.0641	0.0442 ... 0.0561
$\mathcal{N}[3, 64]$	0.0493 ... 0.0528	0.0328 ... 0.0505
$\mathcal{N}[3, 128]$	0.0467 ... 0.0565	0.0336 ... 0.0619
$\mathcal{N}[4, 8]$	0.1030 ... 0.1343	0.0969 ... 0.1050
$\mathcal{N}[4, 16]$	0.0576 ... 0.0729	0.0528 ... 0.0594
$\mathcal{N}[4, 32]$	0.0497 ... 0.0531	0.0381 ... 0.0506
$\mathcal{N}[4, 64]$	0.0475 ... 0.0542	0.0316 ... 0.0460
$\mathcal{N}[4, 128]$	0.0466 ... 0.0505	0.0308 ... 0.0367

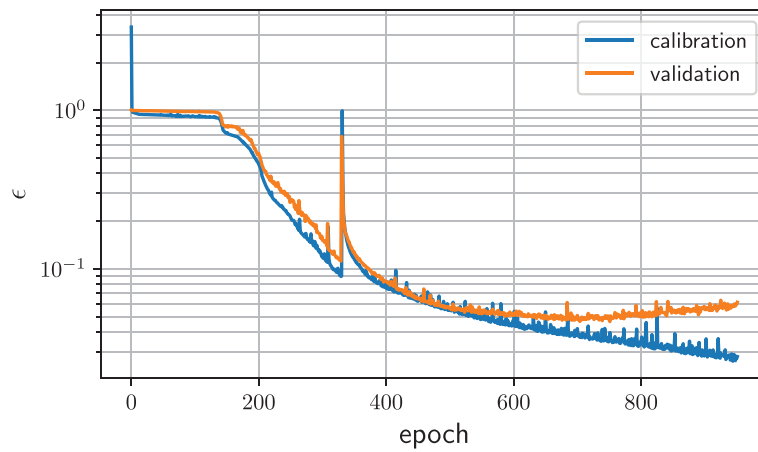


FIGURE 10 Development of ϵ for the best performing instance of $\mathcal{N}[4,128]$ yielding $\epsilon = 0.0466$ for the validation dataset and $\epsilon = 0.0367$ for the calibration dataset

chooses the best performing instance \mathcal{M} with $\mathcal{N}[4,128]$, since a quality saturation with respect to ϵ for D^V seems visible in Table 1 and internal tests with $\mathcal{N}[3,256]$ did not show any major improvement with respect to the validation data.

As a first evaluation of the chosen model \mathcal{M} with $\epsilon = 0.0367$ for D^C and $\epsilon = 0.0466$ for D^V , we consider the cumulative distribution function (cdf) of $\epsilon_{[t,c]}$, compare (35). Its evaluation for D^C and D^V is illustrated in Figure 11 in blue and red, respectively, and the vertical lines correspond to ϵ accordingly. Obviously, the model shows a better performance with respect to D^C with a smaller average (ϵ) and higher initial gradient, compared to D^V . Nevertheless, these cdfs show an acceptable accordance. Hereby, it should be noted again (i) that the model is required to yield good results over 5 orders of magnitude for W and P , compare Figure 9, and (ii) that D^V was specifically designed in order to maximize the distance to D^C in order to obtain a challenging validation set. Based on these considerations, the model is believed to generalize well.

The chosen model \mathcal{M} is now evaluated for selected topologies of the calibration dataset and simulation cases. We consider the topologies $t_1 = (0.125, 0.345, 0.255)$ and $t_2 = (0.995, 0.885, 0.975)$ in order to evaluate a compliant (t_1) and a stiff cell (t_2). Further, in order to make clear the advantages of the newly proposed weights (31) and (32), specially for compliant structures, an additional instance of $\mathcal{N}[4,128]$ is trained with uniform weights equal to 1 with the analogous objective function $(wMSE^W + wMSE^P)/2$. This model is referred to from now on as \mathcal{M}_u . For each topology, t_1 and t_2 , we evaluate for \mathcal{M} and \mathcal{M}_u the simulation cases 1, 2, 7, 8, 15, and 16, corresponding to the tension and compression scenarios for the scenarios 1 (uniaxial), 4 (volumetric), and 8 (uniaxial-shear). The evaluation of the six selected cases for the compliant cell $t_1 = (0.125, 0.345, 0.255)$ is illustrated in Figure 12, while the analogous evaluation for $t_2 = (0.995, 0.885, 0.975)$ is

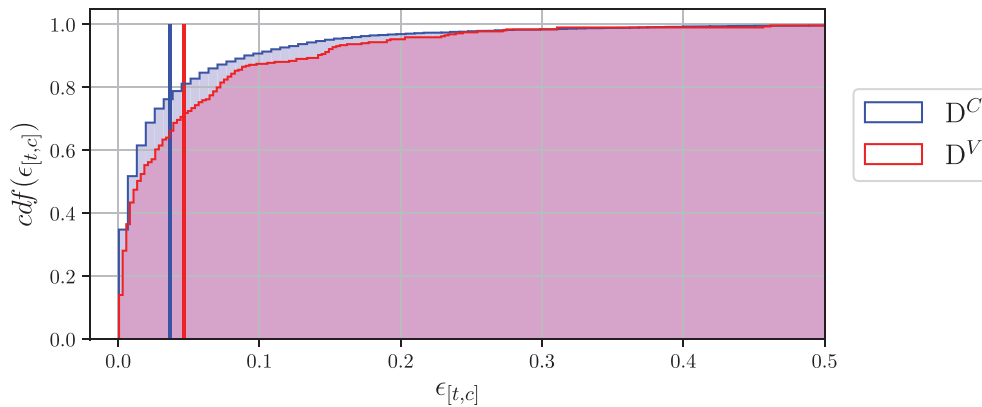


FIGURE 11 Cumulative distribution functions of the error ϵ (truncated up to $\epsilon = 0.5$) of the chosen model \mathcal{M} : calibration dataset D^C (blue) and validation dataset D^V (red); the vertical lines mark the corresponding averages, that is, $\epsilon = 0.0367$ for D^C and $\epsilon = 0.0466$ for D^V

displayed in Figure 13, with \mathcal{M} on the left columns and \mathcal{M}_u on the right columns, respectively. The dotted lines denote the simulation data, while the continuous lines correspond to the evaluations of \mathcal{M} and \mathcal{M}_u . For the sake of a compact illustration, only the stress values $P_{11/12/21/22/33}$ are shown. A more detailed graphical illustration of \mathcal{M} and \mathcal{M}_u showing all stress and potential values is provided in Appendix A.

We first consider the model \mathcal{M} , compare left columns in Figures 12 and 13. The evaluation of the compliant cell with $\underline{t}_1 = (0.125, 0.345, 0.255)$ depicted in Figure 12 shows that \mathcal{M} achieves not only qualitatively but also quantitatively very good results over a wide range of cases. Here, it is important to note that the model is expected to deliver good results for a compliant cell yielding very low values in terms of magnitude for the potential as well as for the stresses. For instance, consider the uniaxial compression and tension cases, illustrated in the first and second rows of Figure 12. In compression, the selected cell yields a maximum absolute value of the stress of around $\max_{s \in S} |P_{ij}| \approx 4$ Pa. Now, consider the uniaxial tension case in the second row, with $\max_{s \in S} |P_{ij}| \approx 40$ Pa. The trained model yields qualitatively satisfactory results for these cases as well as for the uniaxial-shear compression and tension cases (cf. last two rows). For the volumetric case, compare third and fourth row, the model achieves a good agreement with the buckling stress of the perturbed cell, with $\max_{s \in S} |P_{ij}| \approx 4$ Pa, and a good agreement with the stresses in volumetric tension, with $\max_{s \in S} |P_{ij}| \approx 1000$ Pa. Based on these results, already for the compliant cell \underline{t}_1 one can observe that \mathcal{M} yields good results over several order of magnitudes. For immediate comparison, the additional model \mathcal{M}_u trained with uniform weights is displayed in the right column of Figure 12. It can be clearly observed that that \mathcal{M}_u does not achieve the prediction quality of \mathcal{M} , especially for the compression cases and for soft structures (i.e., small values in \underline{t}). This is an implication of the uniform weights, which in $(wMSE^W + wMSE^P)/2$ cannot amplify the errors with values in small orders of magnitude, as for the uniaxial, volumetric and uniaxial-tension compression cases.

The analogous evaluation for the stiff cell with $\underline{t}_2 = (0.995, 0.885, 0.975)$ depicted in Figure 13 further shows not only the good agreement between the model prediction and the calibration data, but also that the model indeed is able to perform well over several orders of magnitude in the output. For instance, consider again the uniaxial compression and tension cases for the compliant and stiff structures in the first and second rows of Figures 12 and 13, respectively. The stress values of these two topologies have a difference of roughly two orders of magnitude. The calibrated model \mathcal{M} is able to achieve a good performance in most cases, showing its flexibility and accuracy over several orders of magnitude in the output space. Only in the volumetric tension case it is clearly visible that \mathcal{M} does not perform accurately for higher load amplitudes. The additional model \mathcal{M}_u shows a good performance for this stiff topology. But this is immediately clear, since the stress values for the stiff topology \underline{t}_2 are orders of magnitude larger than for the compliant topology \underline{t}_1 . These values induce large errors in $(wMSE^W + wMSE^P)/2$, which then dominate the calibration of \mathcal{M}_u .

In summary, it is concluded (i) that the proposed hyperelastic parametric model can generalize well over several order of magnitude for the highly nonlinear buckling behavior of the parametric cells and (ii) that the newly proposed weights (31) and (32) transforming the standard weighted MSE to the relative error ϵ incorporating function (W) and gradient (P) information enhances the prediction quality over the entire range of weak and stiff structures.

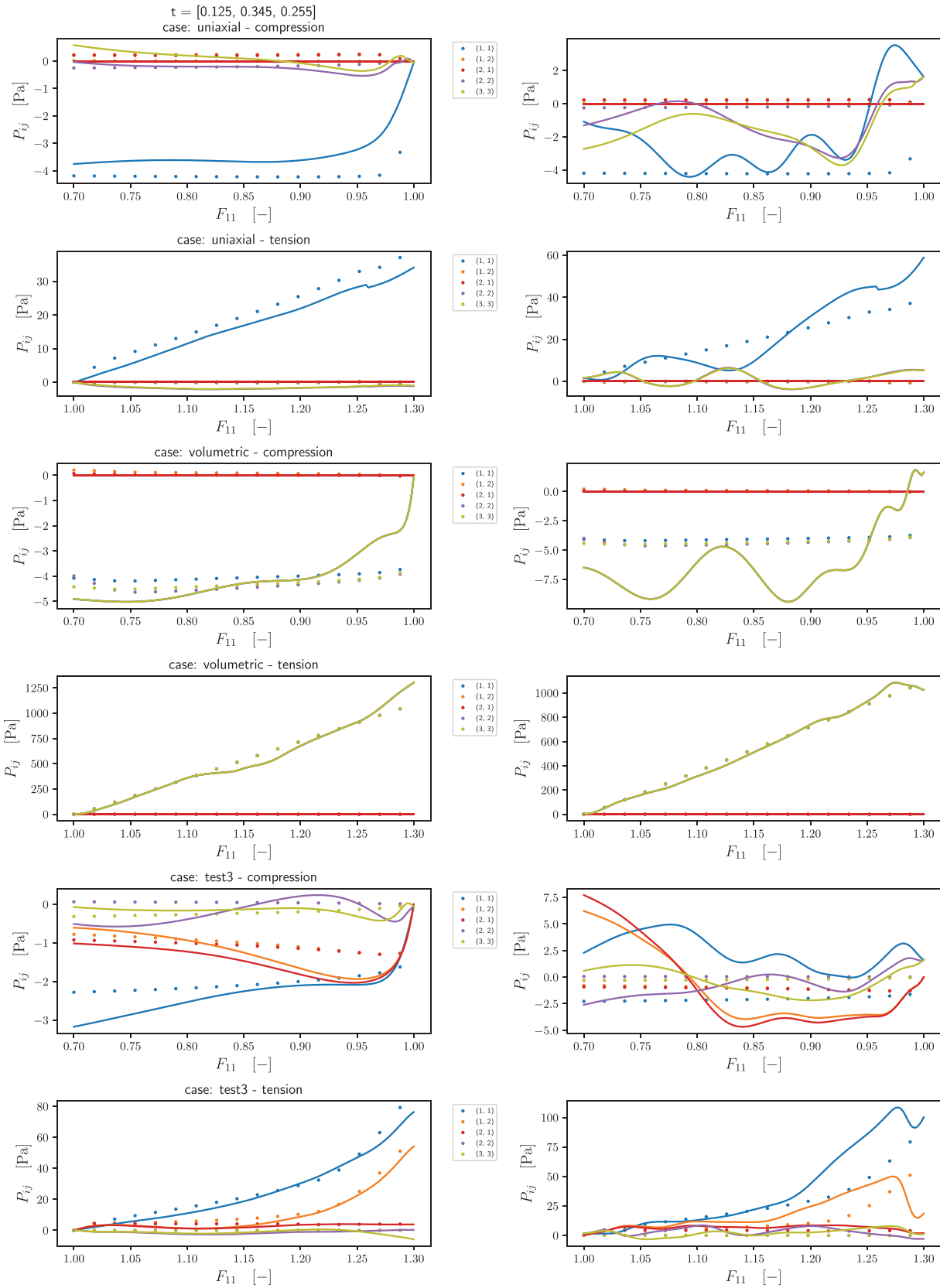


FIGURE 12 Evaluation of trained models with architecture $\mathcal{N}[4,128]$ for $t_1 = (0.125, 0.345, 0.255)$: model trained with newly proposed $wMSE$ with non-uniform weights (left column) and model trained with commonly used uniform weights (right column)

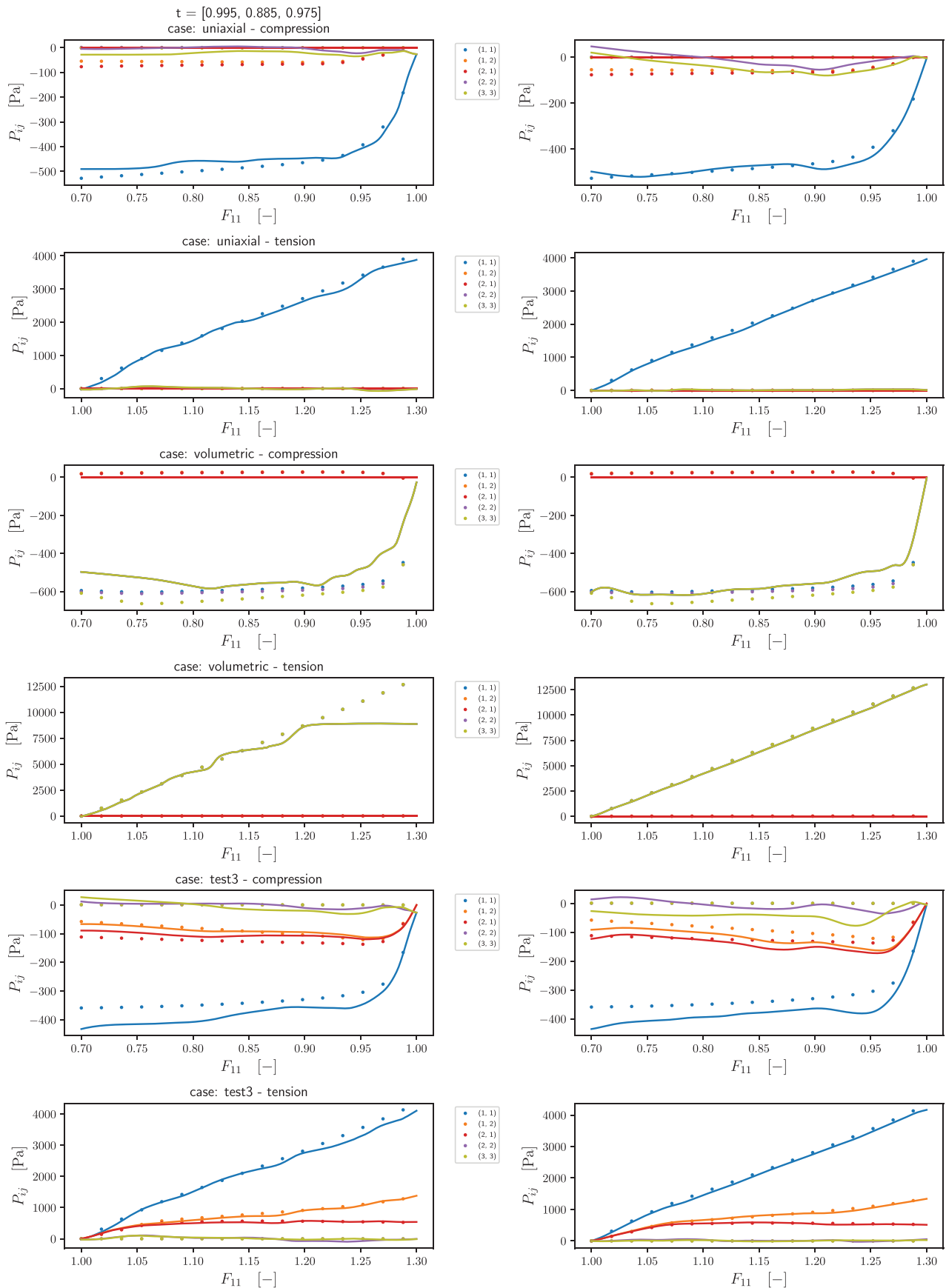


FIGURE 13 Evaluation of trained models with architecture $\mathcal{N}[4,128]$ for $t_2 = (0.995, 0.885, 0.975)$: model trained with newly proposed w MSE with non-uniform weights (left column) and model trained with commonly used uniform weights (right column)

4 | PARAMETRIC MICROSTRUCTURE OPTIMIZATION

A parametric effective constitutive model for a family of microstructures can be used to select a specific microstructure that exhibits a desired constitutive behavior, that is, solve the inverse problem of identifying a suitable parameter set \underline{p} . This can be done by optimizing for \underline{p} , where practical applications would typically require constraints, for example, the range of Young's modulus of available materials or manufacturing related constraints regarding minimal and maximal radius parameters \underline{t} . Here, we demonstrate how the calibrated model $W^{\text{ML}}(\underline{F}, \underline{p})$ (for which we use the best performing instance \mathcal{M} of $\mathcal{N}[4,128]$ from the previous section, compare Figures 12 and 13) can be used to solve such optimization problems and identify the parameter vector $\underline{p} = (E_s, t_1, t_2, t_3)$ of a beam-lattice pRUC that best approximates a given effective behavior.

4.1 | Optimization based on given deformation, energy, and stress

For this first example, we consider the behavior of the pRUC for $\underline{t} = (0.535, 0.065, 0.885)$ in the uniaxial-shear scenario, which is contained in the calibration dataset D^C , but amplified with $E_s = 3$ as the desired objective, for which we want to identify a pRUC that exhibits this uniaxial-shear behavior. The original data and model predictions for $E_s = 1$ are displayed in Figure 14, while the amplified objective behavior is illustrated in Figure 15.

The calibrated model is now used to search for the optimal parameter vector \underline{p} for material and lattice topology based on the given data $\{(\underline{F}_1, W_1, \underline{P}_1), \dots, (\underline{F}_n, W_n, \underline{P}_n)\}$, in this example corresponding to the data displayed in Figure 15 with $n = 2 \cdot \#(S) = 302$, that is, for all simulation steps of the uniaxial-shear scenario, that is, concatenating its compression and tension cases. For that we consider the error function

$$e(\underline{p}) = \frac{1}{n} \sum_{i=1}^n \frac{1}{(\text{J/m}^3)^2} (W_i - W^{\text{ML}}(\underline{F}_i, \underline{p}))^2 + \frac{1}{9 \text{ Pa}^2} \|\underline{P}_i - \underline{P}^{\text{ML}}(\underline{F}_i, \underline{p})\|^2 \quad (36)$$

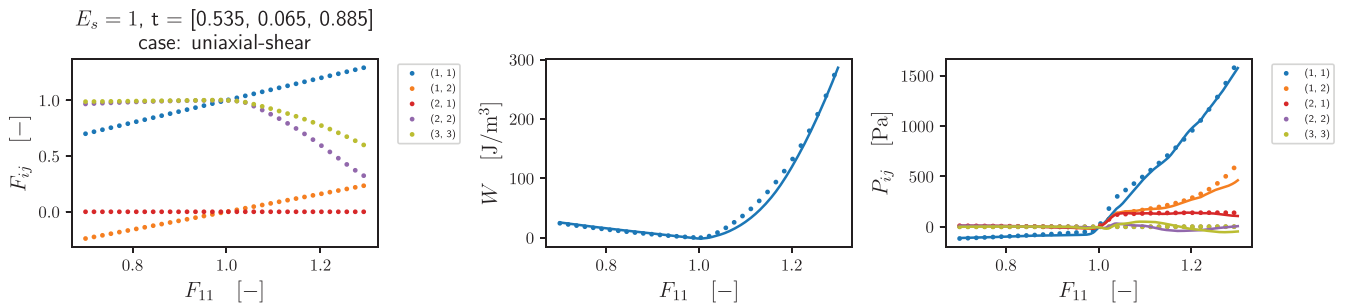


FIGURE 14 Simulated data and model prediction for $\underline{p} = (1.000, 0.535, 0.065, 0.885)$ in the uniaxial-shear case

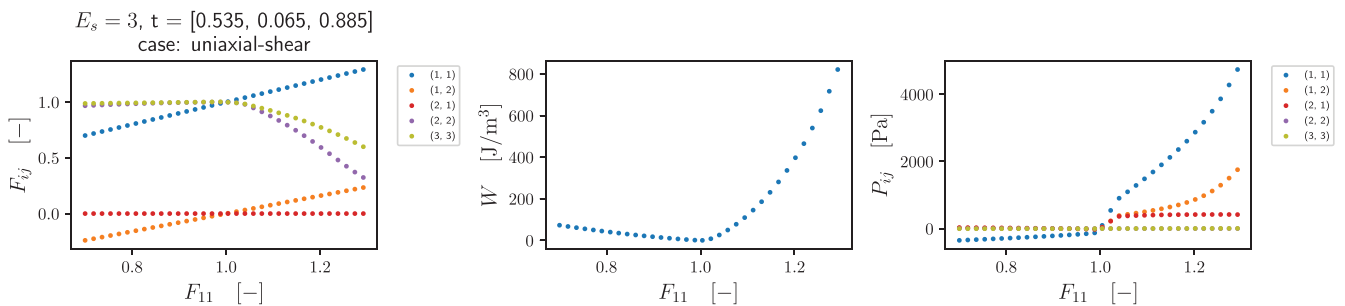


FIGURE 15 Objective data for $\underline{p}^{\text{or}} = (3.000, 0.535, 0.065, 0.885)$ in the uniaxial-shear case

as a pragmatic choice. Alternatively, weights as for the w MSE could be considered, but are not the focus of this example. From a practical perspective, not all materials may be available for production, such that limitations on E_s can be imposed. Therefore, we consider the compact set $\bar{P} = [E_s^-, E_s^+] \times \mathcal{T} \subset P$, compare (13), and the optimization problem

$$\min_{\underline{p} \in \bar{P}} e(\underline{p}). \quad (37)$$

For the current example we set $E_s^- = 0.1$ and $E_s^+ = 10$.

Depending on the optimization algorithm used, algorithms settings and, most importantly, the behavior of the material model, several different acceptable solutions may be found. For instance, in the current example the trivial solution is $\underline{p}^{\text{or}} = (3.000, 0.535, 0.065, 0.885) \in \bar{P}$, which are the parameters used to generate the objective data. However, also other reasonable solution parameters corresponding to local minima of the error function $e(\underline{p})$ may be encountered. For the present example, the initial guess is set to $\underline{p}^0 = (1.0, 0.5, 0.5, 0.5) \in \bar{P}$ and the derivative-free Powell algorithm as implemented in the SciPy package, see Reference 51, in Python 3.8.5 is used. It returns the deviating solution

$$\underline{p}^* = (3.796, 0.520, 0.506, 0.739). \quad (38)$$

The evaluation of the model for the optimized parameters \underline{p}^* is displayed in Figure 16 and a good agreement of the optimized behavior for \underline{p}^* with the desired behavior given by the data for $\underline{p}^{\text{or}}$ can be observed.

4.2 | Optimization based on incomplete data

In some situations information obtained through experimental measurements may be limited, such that, for example, only certain components of the effective deformation and stresses may be accessible and one may have to work with incomplete data. The most basic example for this kind of scenario is the uniaxial stress experiment with explicit measurement of only the F_{11} and P_{11} components. The evaluation of material models solely based on F_{11} is only possible if *assumptions* are made for the remaining deformation components, especially for F_{22} and F_{33} in the uniaxial case for cubic materials. Here, for example, incompressibility may be one option, which may or may not be realistic, depending on the actual material.

If material and/or topology parameters are to be optimized based on a *desired* material behavior solely dictated by F_{11} and P_{11} in a uniaxial tension case, then parametric material models as the one introduced in this work, compare (12), may be used as follows. Given a set of n values $D^{\text{uni}} = \{((F_1)_{11}, (P_1)_{11}), \dots, ((F_n)_{11}, (P_n)_{11})\}$, corresponding to a uniaxial case, the model (12) requires the complete \mathbf{F} and \underline{p} for its evaluation, at what \underline{p} is the later optimization variable. For the pRUC of this work, incompressibility is of course out of question, since the pRUC can be compressed and shows highly nonlinear behavior, for example, in the volumetric compression case. But since simulation data is available, we can use this data as a resource for a second ML model. For the cubic pRUC, for the uniaxial stress state the deformation gradient \mathbf{F}^{uni} is assumed to be represented as

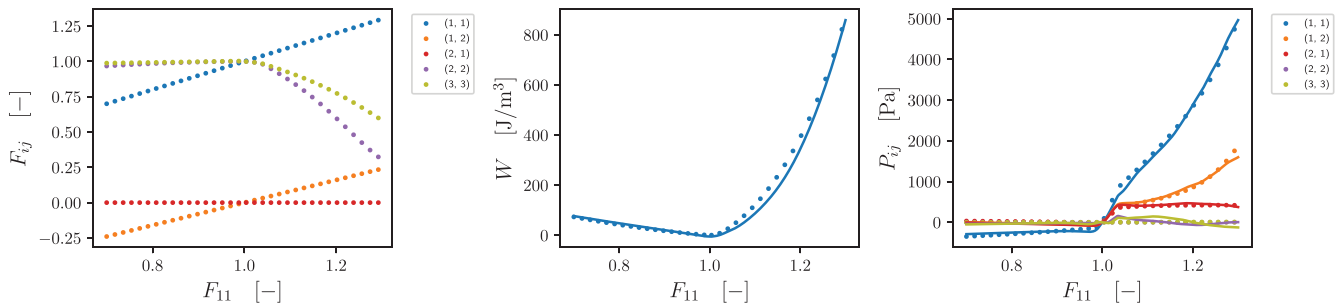


FIGURE 16 Objective data for $\underline{p}^{\text{or}} = (3.000, 0.535, 0.065, 0.885)$ and evaluated model for optimized $\underline{p}^* = (3.796, 0.520, 0.506, 0.739)$ in the uniaxial-shear case

$$\mathbf{F}^{\text{uni}} = \begin{pmatrix} F_{11} & 0 & 0 \\ 0 & \varphi(F_{11}, \underline{p}) & 0 \\ 0 & 0 & \varphi(F_{11}, \underline{p}) \end{pmatrix} \mathbf{e}_i \otimes \mathbf{e}_j, \quad (39)$$

where the function $\varphi(F_{11}, \underline{p})$ represents the parametric dependency of F_{22} and F_{33} on F_{11} (and \underline{p}).

Here, one point requires a short discussion. The deformation behavior of the hyperelastic pRUC of this work has been found to be trivially linear in E . This implies that for any boundary conditions implicitly defining components of the deformation gradient, as in the uniaxial stress state, the implicit dependency of the deformation on the parameters of the pRUC can be reduced to \underline{t} , excluding E_s and, strictly speaking, neglecting the minor dependency on $\nu \geq 0$ as discussed in Section 2.4. The argument is simple, since if \mathbf{F} would implicitly depend on E_s , then the material behavior would *not* be linear in E , which leads to a contradiction. Therefore, the implicit parametric dependency of the deformation is reduced to \underline{t} , not only for the uniaxial stress case, but for any case. This implies that the different deformations of the pRUC can be characterized based on a single material (with reference E_0) and the deformation of any other material (with a different $E = E_s E_0$) is immediately obtainable. Based on this reasoning, we condense the parametric dependency for the uniaxial case to

$$\mathbf{F}^{\text{uni}}(F_{11}, \phi(F_{11}, \underline{t})) = \begin{pmatrix} F_{11} & 0 & 0 \\ 0 & \phi(F_{11}, \underline{t}) & 0 \\ 0 & 0 & \phi(F_{11}, \underline{t}) \end{pmatrix} \mathbf{e}_i \otimes \mathbf{e}_j, \quad (40)$$

from this point on.

This new function $\phi(F_{11}, \underline{t})$ is, of course, difficult to grasp due to the complex behavior depending on \underline{t} . But since simulation data is available, we set up a second ML model for it as $\phi^{\text{ML}}(F_{11}, \underline{t})$, which is trained with data extracted from the dataset D^C used for the calibration of $W^{\text{ML}}(\mathbf{F}, \underline{p})$. The objective function MSE^ϕ for the calibration of ϕ^{ML} is defined as

$$\text{MSE}_{22}^\phi = \frac{1}{\#(\text{T})} \sum_{\underline{t} \in \text{T}} \frac{1}{2} \sum_{c \in \{1,2\}} \frac{1}{\#(\text{S})} \sum_{s \in \text{S}} ((\mathbf{F}_{[\underline{t},c,s]})_{22} - \phi^{\text{ML}}((\mathbf{F}_{[\underline{t},c,s]})_{11}, \underline{t}))^2 \quad (41)$$

$$\text{MSE}_{33}^\phi = \frac{1}{\#(\text{T})} \sum_{\underline{t} \in \text{T}} \frac{1}{2} \sum_{c \in \{1,2\}} \frac{1}{\#(\text{S})} \sum_{s \in \text{S}} ((\mathbf{F}_{[\underline{t},c,s]})_{33} - \phi^{\text{ML}}((\mathbf{F}_{[\underline{t},c,s]})_{11}, \underline{t}))^2 \quad (42)$$

$$\text{MSE}^\phi = \frac{1}{2} (\text{MSE}_{22}^\phi + \text{MSE}_{33}^\phi), \quad (43)$$

where $c \in \{1, 2\}$ refers to the uniaxial tension and compression cases. The function ϕ^{ML} itself is formulated as

$$\phi^{\text{ML}}(F_{11}, \underline{t}) = (1 + (F_{11} - 1)\text{FFNN}(F_{11} - 1, \underline{\tau}))^2 \quad (44)$$

with a FFNN, with the softplus activation function, taking $F_{11} - 1$ and $\tau = \underline{t} - (0.5, 0.5, 0.5)$ as input. The formulation (44) ensures $\phi^{\text{ML}}(1, \underline{t}) = 1$ for all \underline{t} , $\phi^{\text{ML}}(F_{11}, \underline{t}) \geq 0$ for all F_{11} and \underline{t} , and differentiability with respect to F_{11} and \underline{t} . An identical architecture sweep as for the material model has been conducted, that is, a maximum of 3000 epochs is allowed with 500 epochs patience and the objective function is monitored for D^V . The architecture $\mathcal{N}[4,128]$ yielded the best results and is used from this point on.

Now, based on the calibrated ϕ^{ML} , for given set of n values $D^{\text{uni}} = \{((\mathbf{F}_1)_{11}, (\mathbf{P}_1)_{11}), \dots, (\mathbf{F}_n)_{11}, (\mathbf{P}_n)_{11}\}$, the material and topology can be optimized based on a simple composition of the ML models. The F_{11} values can be inserted into ϕ^{ML} to obtain predictions of the unknown F_{22} and F_{33} , for given \underline{t} . Then, these values can be used to build the deformation gradient \mathbf{F}^{uni} , which is then evaluated with given \underline{p} in the W^{ML} model in order to get the stress \mathbf{P}^{ML} . The $(\mathbf{P}^{\text{ML}})_{11}$ component can then be compared to the desired stress value $(\mathbf{P})_{11}$. Thus, we formulate the objective function as

$$e^\phi(\underline{p}) = \frac{1}{n \text{ Pa}^2} \sum_{i=1}^n \left[(\mathbf{P}_i)_{11} - (\mathbf{P}^{\text{ML}}(\mathbf{F}_i^{\text{uni}}(\underline{t}, \underline{p})))_{11} \right]^2, \quad \mathbf{F}_i^{\text{uni}}(\underline{t}) = \mathbf{F}^{\text{uni}}((\mathbf{F}_i)_{11}, \phi^{\text{ML}}((\mathbf{F}_i)_{11}, \underline{t})), \quad (45)$$

and the corresponding optimization problem as

$$\min_{\underline{p} \in \mathbb{P}} e^{\phi}(\underline{p}). \tag{46}$$

In the following, we consider again the parameters of the previous optimization example, namely $\underline{p}^{or} = (3.000, 0.535, 0.065, 0.885)$ with the topology $\underline{t} = (0.535, 0.065, 0.885) \in T$ and material amplification $E_s = 3$, but now for the uniaxial case. The simulated data is displayed in Figure 17.

For the optimization problem of this example, we solely consider the F_{11} and P_{11} values. But it is still of interest, if the ML models provide good predictions of the $F_{22/33}$ and P_{11} values. Evaluation of the given F_{11} and $\underline{t} = (0.535, 0.065, 0.885)$ with the calibrated ϕ^{ML} model yields the black curve displayed in the left plot of Figure 18. The prediction follows closely the data for F_{22} and F_{33} , which deviate only slightly from one another due to the introduced cell perturbations. The corresponding data for P_{11} is illustrated in Figure 18 on the right plot by the blue dotted line. The black line depicts the composition of ϕ^{ML} and W^{ML} , which agrees sufficiently well with the evaluation of W^{ML} based on the original F data (blue line).

Based on these observations, it can be concluded that the optimization problem (46) will have, from a practical point of view, a chance to find at least one acceptable solution, being the original \underline{p}^{or} .

It should be noted that due to the usage of the softplus function, which is infinitely differentiable, in both ML models W^{ML} and ϕ^{ML} , the error function $e^{\phi}(\underline{p})$ is differentiable in \underline{p} , as in the previous optimization example. Thus, in contrast to the previous optimization example, we now use a gradient-based optimization algorithm with constraints for the problem (46). This is easily achievable in Python 3.8.5 with several algorithms from the package SciPy, see Reference 51. Here, we use the Trust Region algorithm with Jacobian information. The Jacobian of $e^{\phi}(\underline{p})$ is easily obtained based on the automatic differentiation routines of TensorFlow 2.4. Starting from $\underline{p}^0 = (1.0, 0.5, 0.5, 0.5)$, the optimization yields the solution

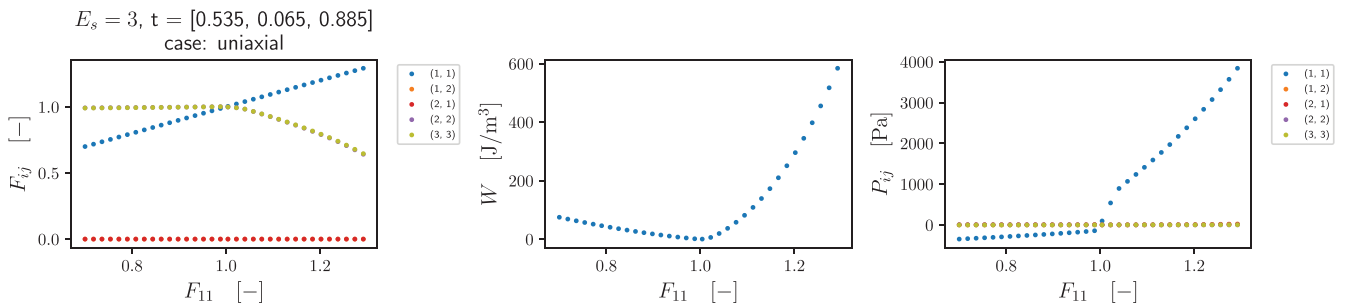


FIGURE 17 Objective data for $\underline{p}^{or} = (3.000, 0.535, 0.065, 0.885)$ in the uniaxial case

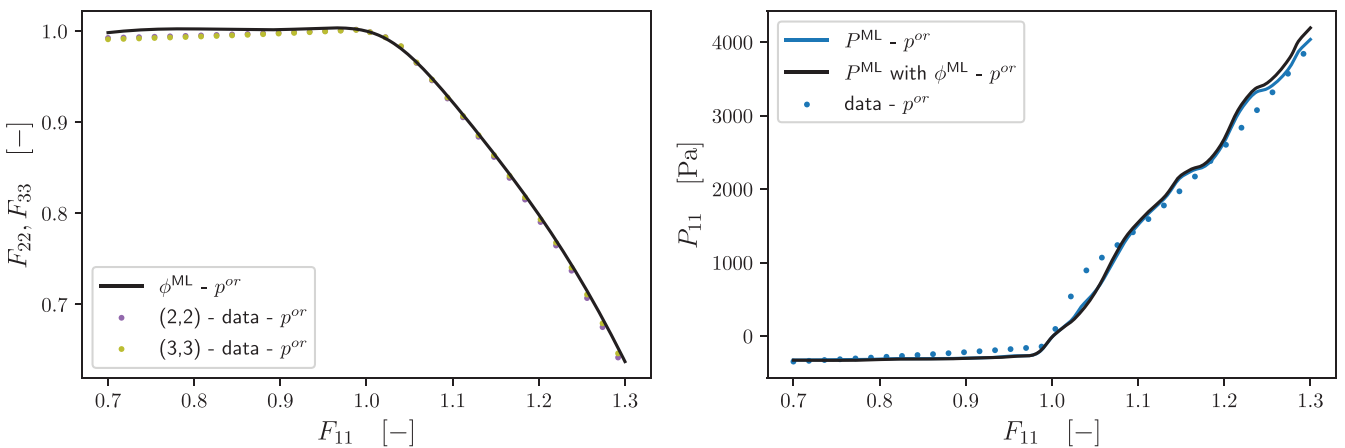


FIGURE 18 Evaluation of data corresponding to $\underline{p}^{or} = (3.000, 0.535, 0.065, 0.885)$. Left: data for F_{22} (purple, dotted), F_{33} (olive, dotted) and prediction of calibrated ϕ^{ML} (black). Right: data for P_{11} (blue, dotted), predictions based on the full F with W^{ML} and corresponding P^{ML} (blue) and predictions based on F_{11} and ϕ^{ML} evaluated then with W^{ML} and corresponding P^{ML} (black)

$$\underline{p}^* = (1.299, 0.979, 0.429, 0.587). \tag{47}$$

Evaluation of the model composition for the optimized parameters \underline{p}^* is depicted in Figure 19 in red. It can be observed, that for \underline{p}^* the predicted behavior of F_{22} and F_{33} (red line) deviates significantly from the behavior for \underline{p}^{or} (dotted lines), compare the left plot in Figure 19. Nevertheless, it still yields a stress behavior very close to the desired one, compare right plot in Figure 19. The pRUC corresponding to \underline{p}^* was not contained in the calibration dataset D^C and has been simulated for verifying the results. The corresponding new data is illustrated by the dashed-dotted lines in Figure 19. It can be seen that ϕ^{ML} predicts qualitatively well the F_{22} and F_{33} behavior for the cell corresponding to \underline{p}^* , compare left plot. The trend of the P_{11} stress for \underline{p}^* is fairly close to the one for \underline{p}^{or} , compare right plot. Evaluation of the W^{ML} model with the F values collected from the new simulation yields the orange curve shown in the right plot of Figure 19. It can be seen that the composition of the models (red curve) and the evaluation of W^{ML} based on the exact deformation (orange curve) are very close the each other. Further, all stress component based on the ML model composition and the optimized parameters \underline{p}^* are depicted in Figure 20, corresponding to the red curves of Figure 19. Here, it should be noted that model evaluation through the composition of ϕ^{ML} and W^{ML} yields a uniaxial stress state, to a reasonable degree, even though neither $P_{22} = 0$

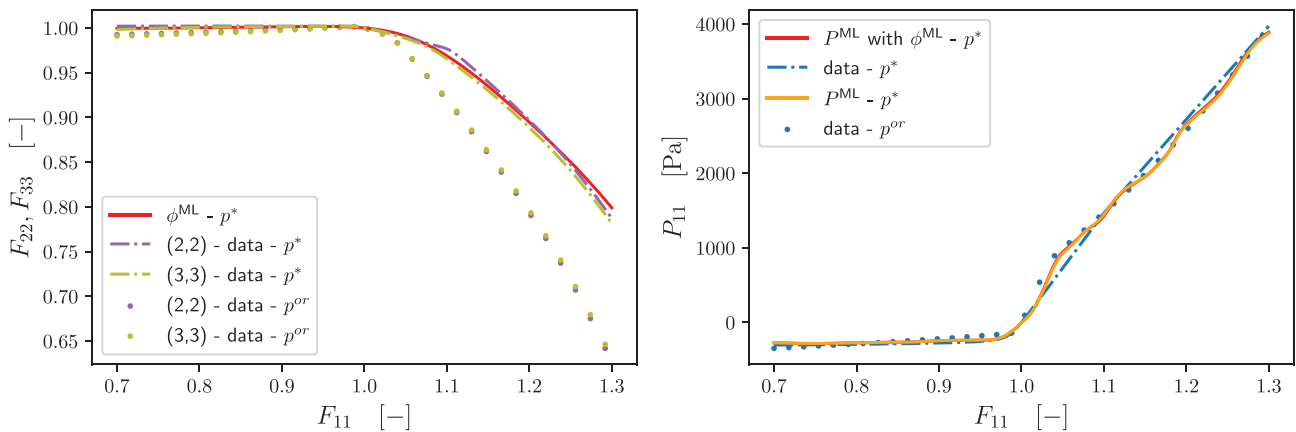


FIGURE 19 Evaluation of data and models corresponding to \underline{p}^{or} and \underline{p}^* : Left: data for F_{22} for \underline{p}^{or} (purple, dotted), F_{33} for \underline{p}^{or} (olive, dotted), prediction of calibrated ϕ^{ML} for \underline{p}^* (red), data for F_{22} for \underline{p}^* (purple, dashed-dotted) and data for F_{33} for \underline{p}^* (olive, dashed-dotted); Right: data for P_{11} for \underline{p}^{or} (blue, dotted), predictions for \underline{p}^* based on F_{11} and ϕ^{ML} evaluated then with W^{ML} and corresponding P^{ML} (red), data for P_{11} for \underline{p}^* (blue, dashed-dotted) and predictions for \underline{p}^* based on the full F with W^{ML} and corresponding P^{ML} (orange)

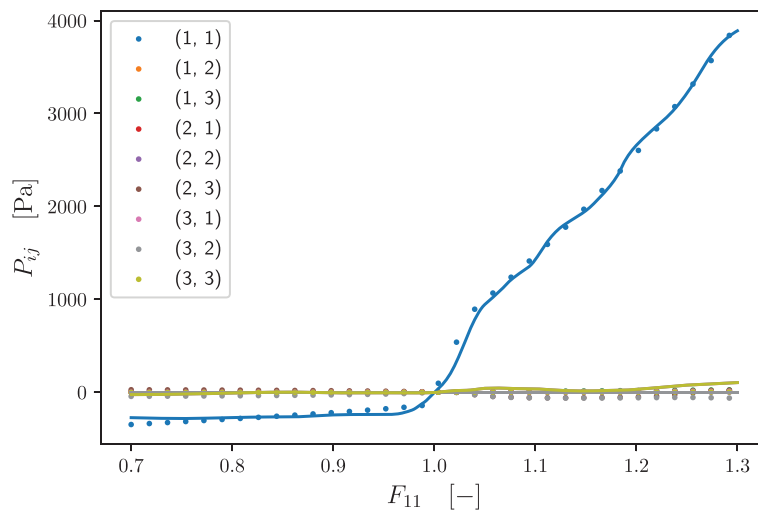


FIGURE 20 Evaluation of all stress components: objective data (dotted lines), model evaluation (continuous lines) based on the calibrated ϕ^{ML} and the optimized parameters \underline{p}^* , corresponding to the red lines in Figure 19

nor $P_{33} = 0$ were imposed in the objective function (45). This is due to the reasonable approximation of the corresponding uniaxial path in the deformation space, see Figure 19.

Depending on pragmatic tolerances on the desired (F_{11}, P_{11}) behavior, the obtained solution \underline{p}^* may offer an acceptable compromise obtained through the calibrated ML models. Of course, further improvements could be achieved, for example, by accumulation of more training data for the ML models or a weighting of crucial points of the desired (F_{11}, P_{11}) behavior. This may be important for some applications, since in the present example the behavior in the vicinity of the undeformed state contributes smaller error values in the objective function (45), compared to values for large tension. The present approach simply showcases that, in principle, the calibrated material model W^{ML} can be used in combination with further ML models for optimization problems with incomplete data.

5 | CONCLUSIONS

The present work presents an anisotropic, hyperelastic constitutive modeling approach for parametric nonlinear metamaterials and demonstrates its application to beam lattice microstructures and their optimization. For this purpose, the machine learning-based method of Reference 38 is extended by including the parametric dependencies into the FFNN formulation in a straight-forward and non-intrusive fashion.

In view of the computational performance the most relevant statements are (i) that the evaluation of the machine learned model has an explicitly and a priori known computational cost, (ii) arbitrary load states in the admissible range can directly be evaluated without running a simulation involving small load increments and (iii) the computational cost is independent of the resolution of the discrete pRUC model and, generally, distinctly lower. We are not providing speed-up information as the latter would depend heavily on software, hardware and so forth.

As an example of a parametric metamaterial, a highly nonlinear cubic beam-lattice microstructure is investigated, for which topology and morphology are controlled using three parameters. The influence of material parameters due to modeling assumptions is examined and the dominance of the lattice parameters has been shown. Based on these observations, the parametric anisotropic hyperelastic material model is formulated as a FFNN. The model is trained on a fairly sparse and pragmatic data generation strategy with corresponding sample weighting connecting the weighted MSE with a sensible relative error measure depending on the cell topology and loading case. The objective function ϵ incorporates potential and stress information and forces the model to yield good predictions for stiff and compliant structures in tension and compression loading cases. The complete calibration dataset is made openly accessible by the authors through the GitHub repository <https://github.com/CPSHub/sim-data>.

The calibrated model is then showcased in two optimization problems, in which the material and the topology of the parametric metamaterial are tailored for a desired nonlinear behavior. The first example concerns the identification optimal cell parameters based on fully prescribed deformation, energy and stress data. Here, it is demonstrated that the calibrated model works well with standard, gradient-free optimization algorithms. In the second example, incomplete data is prescribed for the uniaxial behavior in terms of (F_{11}, P_{11}) . For this scenario, an auxiliary machine learning model is trained for predicting the deformation behavior for uniaxial deformation and then coupled with the full model. Here, a gradient-based optimization algorithm is used, which demonstrates the versatility of the proposed material modeling approach, since not only the stresses can be obtained from the neural network-based strain energy density W through automatic differentiation ($\mathbf{P} = \partial W / \partial \mathbf{F}$), but also the gradients with respect to the lattice parameters (e.g., $\partial \mathbf{P} / \partial \underline{p} = \partial^2 W / \partial \mathbf{F} \partial \underline{p}$).

In principle, the constitutive modeling approach introduced in this work can be applied to any kind of nonlinear elastic (meta-) material with a known class of material symmetry, for which parametric dependency is of interest, for example, fiber-reinforced composites, multi-material microstructures, open- and closed-cell foams, bio-materials, textiles, and so forth. It facilitates the investigation of micro-macro topology optimization, in which an effective constitutive model can be used on the macro level. In this way, topology optimization algorithms can make use of the present work and optimize not only the macroscopic material distribution, but also a micro-parameter field, corresponding to \underline{p} . This would enable future macroscopic parts with varying, highly dedicated material and topology at the micro level.

As pointed out in Section 1, the present approach assumes that the material behavior is well approximated by a state-dependent hyperelastic model. The investigation carried out in Section 2.3 and the evaluation of the calibrated models support the assumption for the structures and range of material parameters taken into consideration. Nevertheless, other structures and a wider range of material parameters and perturbations may show higher discrepancies and violate

many homogenization assumptions. Future work could concentrate on a dedicated investigation of these aspects, while pragmatic approaches could consider the present work as a starting point for parametric structures in the meantime.

ACKNOWLEDGMENTS

Mauricio Fernández and Oliver Weeger would like to acknowledge the support from the Department of Mechanical Engineering at TU Darmstadt. The contributions by Felix Fritzen are funded by Deutsche Forschungsgemeinschaft (DFG, German Research Foundation) within the scope of the Heisenberg program—project number 406068690, Grant FR2702/8—and under Germany's Excellence Strategy—EXC 2075—390740016. Felix Fritzen acknowledges the support by the Stuttgart Center for Simulation Science (SimTech). Further, the authors thank the unknown reviewers for their comments and suggestions, which helped to improve the quality of the approach taken.

AUTHOR CONTRIBUTIONS


Mauricio Fernández and **Oliver Weeger** designed the research scope. **Mauricio Fernández** and **Oliver Weeger** carried out the cell simulations. **Mauricio Fernández**, **Oliver Weeger**, and **Felix Fritzen** developed the machine learning model and training approach. **Mauricio Fernández** implemented, trained and evaluated the parametric material model, designed and carried out the optimization examples, and created the repository for the openly accessible calibration data. **Mauricio Fernández**, **Felix Fritzen**, and **Oliver Weeger** wrote and proof-read the manuscript.

DATA AVAILABILITY STATEMENT

The data that support the findings of this study are available at the GitHub repository <https://github.com/CPSHub/sim-data> under the CC-BY-4.0 license.

ORCID

Mauricio Fernández  <https://orcid.org/0000-0003-1840-1243>

Felix Fritzen  <https://orcid.org/0000-0003-4926-0068>

Oliver Weeger  <https://orcid.org/0000-0002-1771-8129>

REFERENCES

1. Wegener M. Metamaterials beyond optics. *Science*. 2013;342(6161):939-940. doi:10.1126/science.1246545
2. Jia Z, Liu F, Jiang X, Wang L. Engineering lattice metamaterials for extreme property, programmability, and multifunctionality. *Journal of Applied Physics*. 2020;127(15):150901. doi:10.1063/5.0004724
3. Coulais C, Teomy E, de Reus K, Shokef Y, van Hecke M. Combinatorial design of textured mechanical metamaterials. *Nature*. 2016;535(7613):529-532. doi:10.1038/nature18960
4. Qu J, Kadic M, Naber A, Wegener M. Micro-structured two-component 3D metamaterials with negative thermal-expansion coefficient from positive constituents. *Sci Rep*. 2017;7(1):40643. doi:10.1038/srep40643
5. Schumacher C, Bickel B, Rys J, Marschner S, Daraio C, Gross M. Microstructures to control elasticity in 3D printing. *ACM Trans Graph (TOG)*. 2015;34(4):136.
6. Boddeti N, Ding Z, Kaijima S, Maute K, Dunn ML. Simultaneous digital design and additive manufacture of structures and materials. *Sci Rep*. 2018;8(1):15560. doi:10.1038/s41598-018-33454-3
7. Watts S, Arrighi W, Kudo J, Tortorelli DA, White DA. Simple, accurate surrogate models of the elastic response of three-dimensional open truss micro-architectures with applications to multiscale topology design. *Structural and Multidisciplinary Optimization*. 2019;60(5):1887-1920. doi:10.1007/s00158-019-02297-5
8. Kumar S, Tan S, Zheng L, Kochmann DM. Inverse-designed spinodoid metamaterials. *Npj Comput Mater*. 2020;6(1):1-10. doi:10.1038/s41524-020-0341-6
9. Andersen MN, Wang F, Sigmund O. On the competition for ultimately stiff and strong architected materials. *Mater Des*. 2021;198:109356. doi:10.1016/j.matdes.2020.109356
10. Clausen A, Wang G, Jensen JS, Sigmund O, Lewis JA. Topology optimized architectures with programmable Poisson's ratio over large deformations. *Adv Mater*. 2015;27(37):5523-5527.
11. Bertoldi K, Vitelli V, Christensen J, van Hecke M. Flexible mechanical metamaterials. *Nature Rev Mater*. 2017;2(11):1-11. doi:10.1038/natrevmats.2017.66
12. Bodaghi M, Liao WH. 4D printed tunable mechanical metamaterials with shape memory operations. *Smart Mater Struct*. 2019;28(4):045019. doi:10.1088/1361-665X/ab0b6b
13. Soyarslan C, Blümer V, Bargmann S. Tunable auxeticity and elastomechanical symmetry in a class of very low density core-shell cubic crystals. *Acta Mater*. 2019;177:280-292. doi:10.1016/j.actamat.2019.07.015
14. Li X, Yang Z, Lu Z. Design 3D metamaterials with compression-induced-twisting characteristics using shear-compression coupling effects. *Extreme Mech Lett*. 2019;29:100471. doi:10.1016/j.eml.2019.100471

15. Liu J, Yan D, Zhang Y. Mechanics of unusual soft network materials with rotatable structural nodes. *J Mech Phys Solids* 2021; 146(September 2020): 104210. doi: 10.1016/j.jmps.2020.104210
16. Jamshidian M, Boddeti N, Rosen D, Weeger O. Multiscale modelling of soft lattice metamaterials: micromechanical non-linear buckling analysis, experimental verification, and macroscale constitutive behaviour. *Int J Mech Sci.* 2020;188:105956. doi:10.1016/j.ijmecsci.2020.105956
17. Pal RK, Ruzzene M, Rimoli JJ. A continuum model for nonlinear lattices under large deformations. *Int J Solids Struct.* 2016;96:300-319. doi:10.1016/j.ijsolstr.2016.05.020
18. ElNady K, Goda I, Ganghoffer JF. Computation of the effective nonlinear mechanical response of lattice materials considering geometrical nonlinearities. *Comput Mech.* 2016;58(6):957-979. doi:10.1007/s00466-016-1326-7
19. Glaesener RN, Lestringant C, Telgen B, Kochmann DM. Continuum models for stretching- and bending-dominated periodic trusses undergoing finite deformations. *Int J Solids Struct.* 2019;171:117-134. doi:10.1016/j.ijsolstr.2019.04.022
20. Glaesener RN, Träff EA, Telgen B, Canonica RM, Kochmann DM. Continuum representation of nonlinear three-dimensional periodic truss networks by on-the-fly homogenization. *Int J Solids Struct.* 2020;206:101-113.
21. Xia L, Breitkopf P. Recent advances on topology optimization of multiscale nonlinear structures. *Arch Comput Methods Eng.* 2017;24(2):227-249. doi:10.1007/s11831-016-9170-7
22. Fritzen F, Xia L, Leuschner M, Breitkopf P. Topology optimization of multiscale elastoviscoplastic structures. *Int J Numer Methods Eng.* 2016;106(6):430-453. doi:10.1002/nme.5122
23. Le BA, Yvonnet J, He QC. Computational homogenization of nonlinear elastic materials using neural networks. *Int J Numer Methods Eng.* 2015;104(12):1061-1084.
24. Ibañez R, Borzacchiello D, Aguado JV, et al. Data-driven non-linear elasticity: constitutive manifold construction and problem discretization. *Comput Mech.* 2017;60(5):813-826.
25. Fritzen F, Fernández M, Larsson F. On-the-fly adaptivity for nonlinear twoscale simulations using artificial neural networks and reduced order modeling. *Front Mater.* 2019;6(75):1-18. doi:10.3389/fmats.2019.00075
26. Nguyen LTK, Keip MA. A data-driven approach to nonlinear elasticity. *Comput Struct.* 2018;194:97-115.
27. Ling J, Jones R, Templeton J. Machine learning strategies for systems with invariance properties. *J Comput Phys.* 2016;318:22-35. doi:10.1016/j.jcp.2016.05.003
28. Yang H, Guo X, Tang S, Liu WK. Derivation of heterogeneous material laws via data-driven principal component expansions. *Comput Mech.* 2019;64(2):365-279. doi:10.1007/s00466-019-01728-w
29. González D, Chinesta F, Cueto E. Learning corrections for hyperelastic models from data. *Front Mater.* 2019;6. doi:10.3389/fmats.2019.00014
30. González D, García-González A, Chinesta F, Cueto E. A data-driven learning method for constitutive modeling: application to vascular hyperelastic soft tissues. *Materials (Basel).* 2020;13(10):1-17. doi:10.3390/ma13102319
31. Chung I, Im S, Cho M. A neural network constitutive model for hyperelasticity based on molecular dynamics simulations. *Int J Numer Methods Eng.* 2021;122(1):5-24. doi:10.1002/nme.6459
32. Fritzen F, Kunc O. Two-stage data-driven homogenization for nonlinear solids using a reduced order model. *Eur J Mech A / Solids.* 2018;69:201-220. doi:10.1016/j.euromechsol.2017.11.007
33. Yvonnet J, Gonzalez D, He QC. Numerically explicit potentials for the homogenization of nonlinear elastic heterogeneous materials. *Comput Methods Appl Mech Eng.* 2009;198(33-36):2723-2737. doi:10.1016/j.cma.2009.03.017
34. Kunc O, Fritzen F. Generation of energy-minimizing point sets on spheres and their application in mesh-free interpolation and differentiation. *Adv Comput Math.* 2019;45(5-6):3012-3065. doi:10.1007/s10444-019-09726-5
35. Kunc O, Fritzen F. Many-scale finite strain computational homogenization via concentric interpolation. *Int J Numer Methods Eng.* 2020;121(21):4689-4716. doi:10.1002/nme.6454
36. Minh Nguyen-Thanh V, Trong Khiem Nguyen L, Rabczuk T, Zhuang X. A surrogate model for computational homogenization of elastostatics at finite strain using high-dimensional model representation-based neural network. *Int J Numer Methods Eng.* 2020;121(21):4811-4842. doi:10.1002/nme.6493
37. Vlassis N, Ma R, Sun W. geometric deep learning for computational mechanics part I: anisotropic hyperelasticity. *Comput Methods Appl Mech Eng.* 2020;371:113299. doi:10.1016/j.cma.2020.113299
38. Fernández M, Jamshidian M, Böhlke T, Kersting K, Weeger O. Anisotropic hyperelastic constitutive models for finite deformations combining material theory and data-driven approaches with application to cubic lattice metamaterials. *Comput Mech.* 2021;67(2):653-677. doi:10.1007/s00466-020-01954-7
39. Bickel B, Bächer M, Otaduy MA, et al. Design and fabrication of materials with desired deformation behavior. *Trans Graph (TOG).* 2010;29:63.
40. Ma C, Zhang Z, Luce B, et al. Accelerated design and characterization of non-uniform cellular materials via a machine-learning based framework. *Npj Comput Mater.* 2020;6(1):1-8. doi:10.1038/s41524-020-0309-6
41. Weeger O, Yeung SK, Dunn M. Isogeometric collocation methods for Cosserat rods and rod structures. *Comput Methods Appl Mech Eng.* 2017;316:100-122. doi:10.1016/j.cma.2016.05.009
42. Weeger O, Boddeti N, Yeung SK, Kaijima S, Dunn M. Digital design and nonlinear simulation for additive manufacturing of soft lattice structures. *Addit Manuf.* 2019;25:39-49. doi:10.1016/j.addma.2018.11.003
43. Riks E. An incremental approach to the solution of snapping and buckling problems. *Int J Solids Struct.* 1979;15(7):529-551. doi:10.1016/0020-7683(79)90081-7

44. Potier-Ferry M. Foundations of elastic postbuckling theory. In: Arbocz J, Potier-Ferry M, Singer J, Tvergaard V, eds. *Buckling and Post-Buckling: Four Lectures in Experimental, Numerical and Theoretical Solid Mechanics Based on Talks Given at the CISM-Meeting Held in Udine, Italy, September 29–October 3, 1985* *Lecture Notes in Physics*. Springer; 1987:1-82.
45. Casciaro R, Garcea G, Attanasio G, Giordano F. Perturbation approach to elastic post-buckling analysis. *Comput Struct*. 1998;66(5):585-595. doi:10.1016/S0045-7949(97)00112-0
46. Truesdell C, Noll W, Antman SS. *The Non-Linear Field Theories of Mechanics*. 3rd ed. Springer; 2004.
47. Šilhavý M. *The Mechanics and Thermodynamics of Continuous Media*. Springer; 1997.
48. Cotton FA. *Chemical Applications of Group Theory*. 3rd. ed. Wiley; 1990.
49. Coleman BD, Noll W. Material symmetry and thermostatic inequalities in finite elastic deformations. *Arch Ration Mech Anal*. 1964;15(2):87-111. doi:10.1007/BF00249520
50. Leuschner M, Fritzen F. Reduced order homogenization for viscoplastic composite materials including dissipative imperfect interfaces. *Mech Mater*. 2017;104:121-138. doi:10.1016/j.mechmat.2016.10.008
51. Virtanen P, Gommers R, Oliphant TE, et al. SciPy 1.0: fundamental algorithms for scientific computing in Python. *Nature Methods*. 2020;17(3):261-272. doi:10.1038/s41592-019-0686-2

How to cite this article: Fernández M, Fritzen F, Weeger O. Material modeling for parametric, anisotropic finite strain hyperelasticity based on machine learning with application in optimization of metamaterials. *Int J Numer Methods Eng*. 2022;123(2):577-609. doi: 10.1002/nme.6869

APPENDIX A. DETAILED EVALUATION OF BEST PERFORMING MODELS

The chosen model instance \mathcal{M} with $\mathcal{N}[4,128]$ and calibrated with the newly proposed weights (31) and (32) illustrated in the left columns of Figures 12 and 13 is shown with further details in Figures A1 and A2. The left columns show the components of the deformation gradient, the middle columns correspond to the potential values and the right columns illustrate the stresses. The analogous evaluation for the model \mathcal{M}_u with uniform weights is shown in Figures A3 and A4.

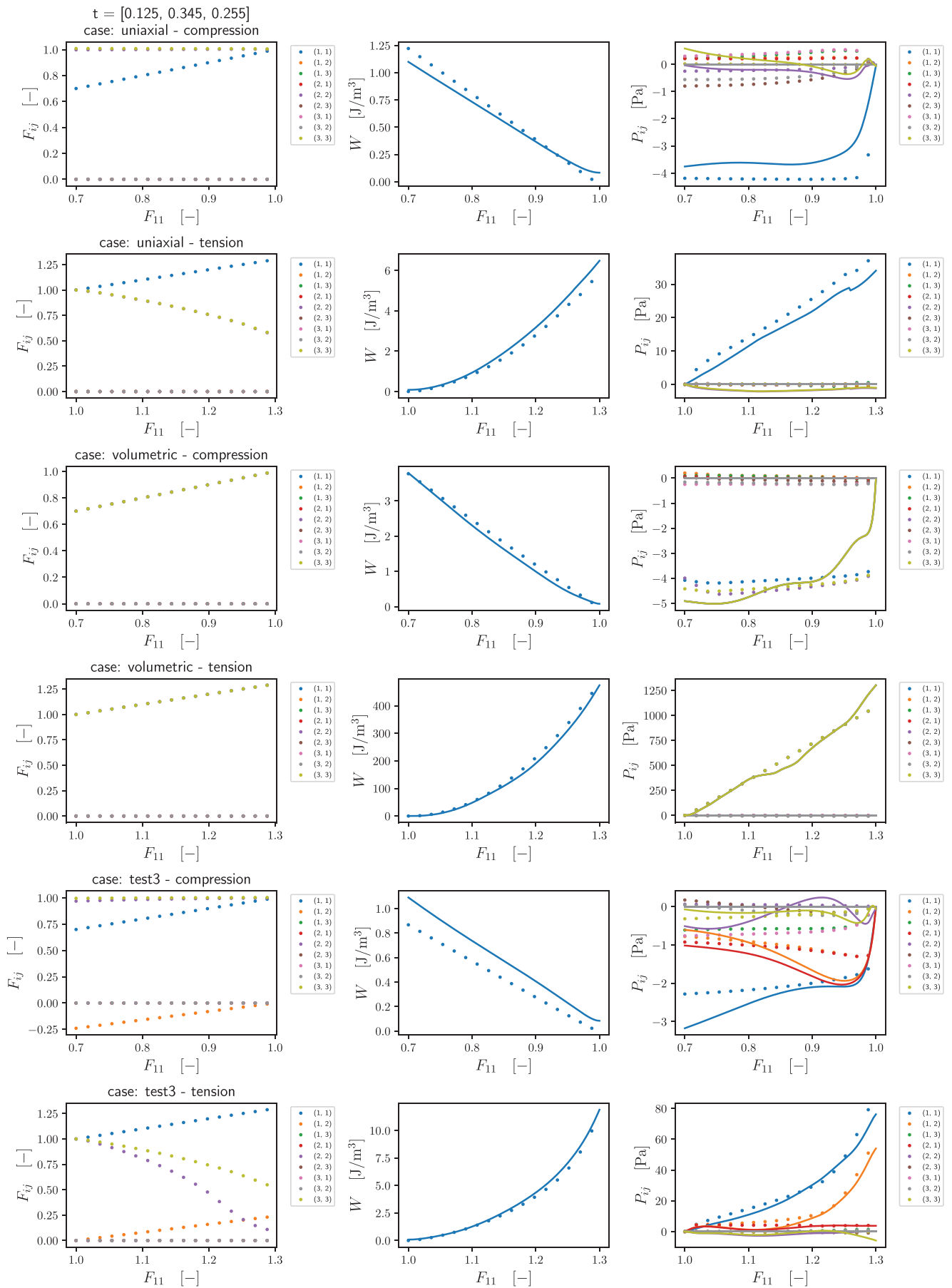


FIGURE A1 Evaluation of trained model \mathcal{M} based on network $\mathcal{N}[4,128]$ and ϵ for $t_1 = (0.125, 0.345, 0.255)$

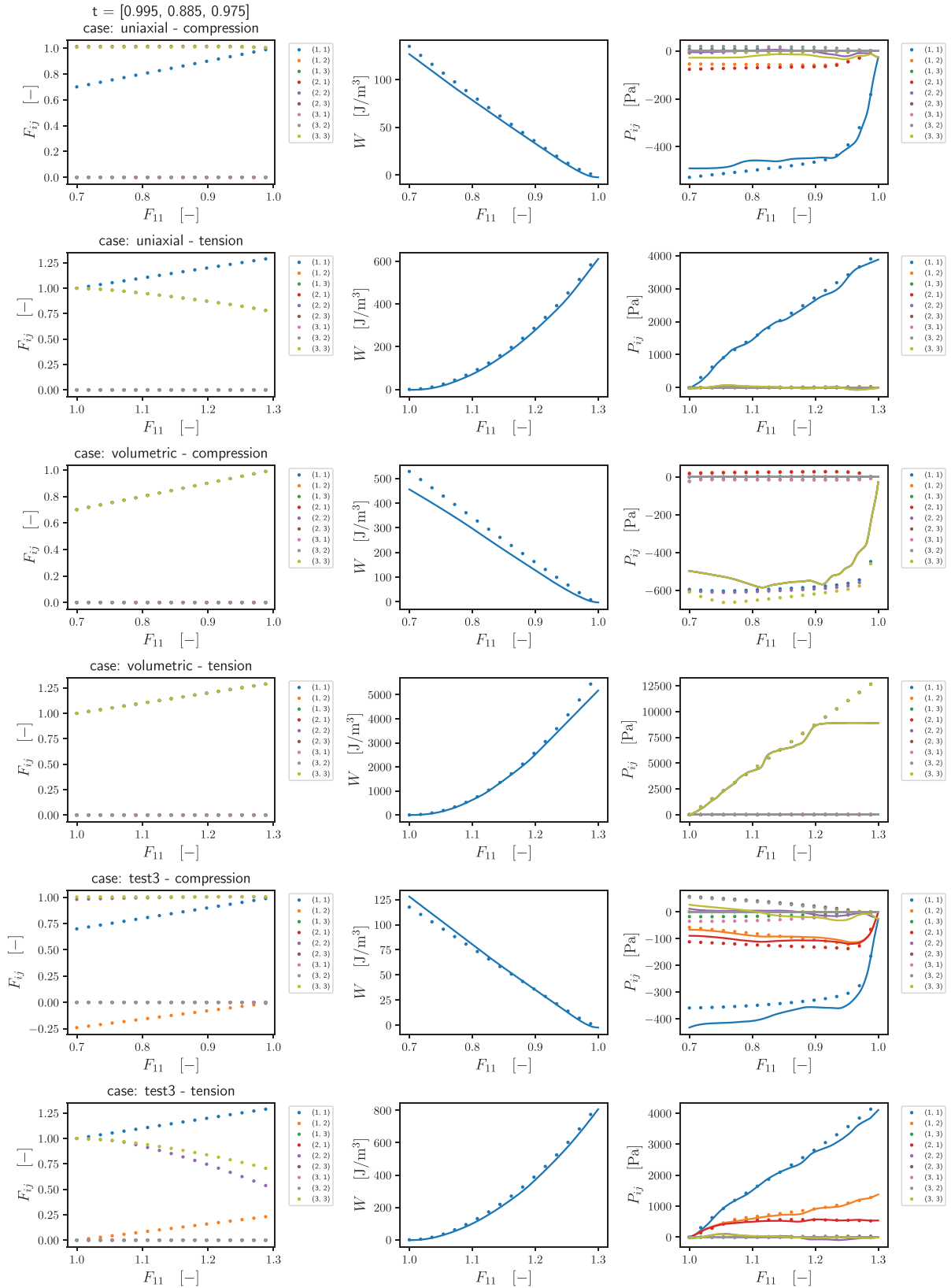


FIGURE A2 Evaluation of trained model \mathcal{M} based on network $\mathcal{N}[4,128]$ and ϵ for $t_2 = (0.995, 0.885, 0.975)$

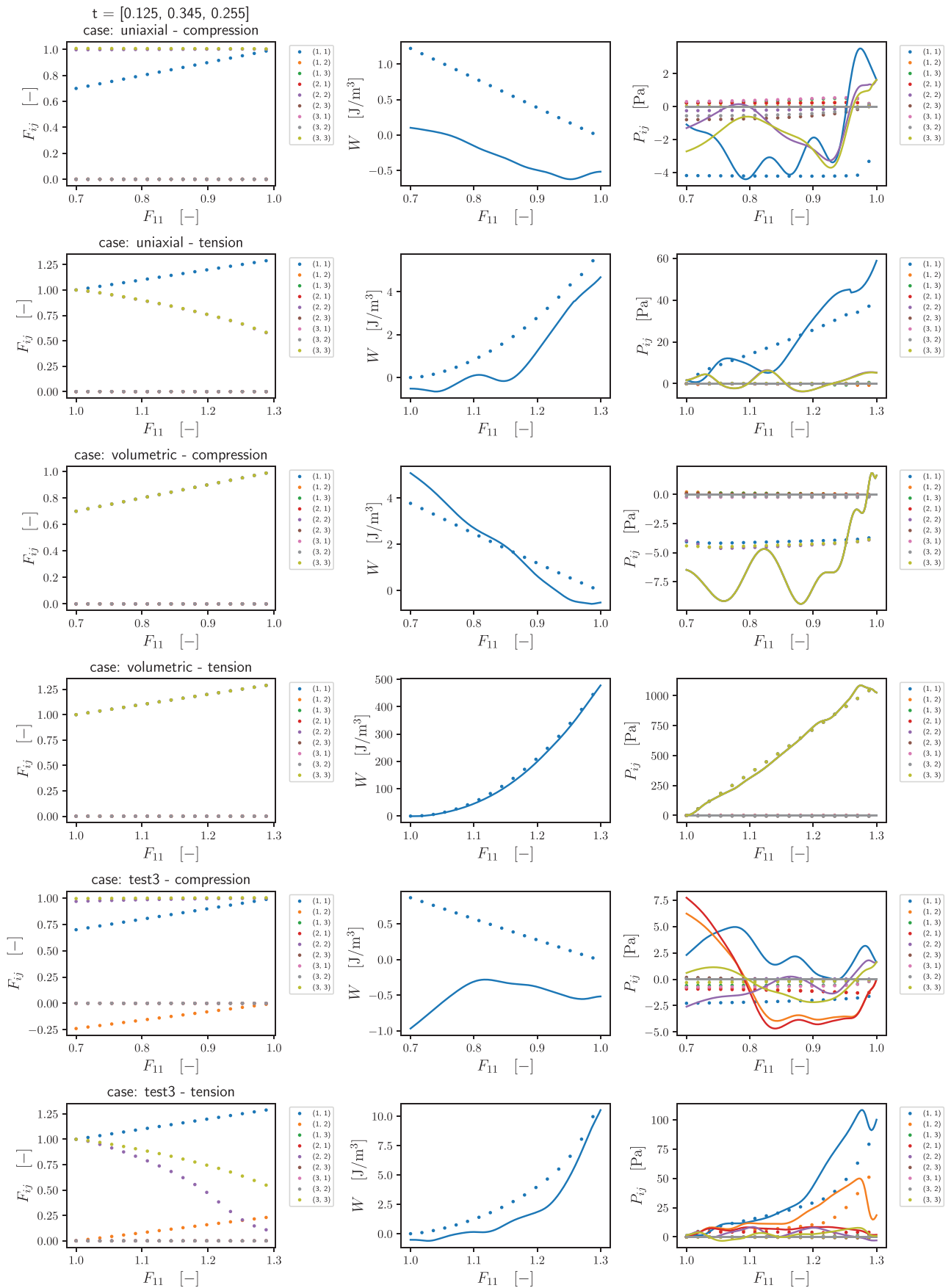


FIGURE A3 Evaluation of trained model \mathcal{M}_u based on network $\mathcal{N}[4,128]$ and $(wMSE^W + wMSE^P)/2$ with uniform weights for $t_1 = (0.125, 0.345, 0.255)$

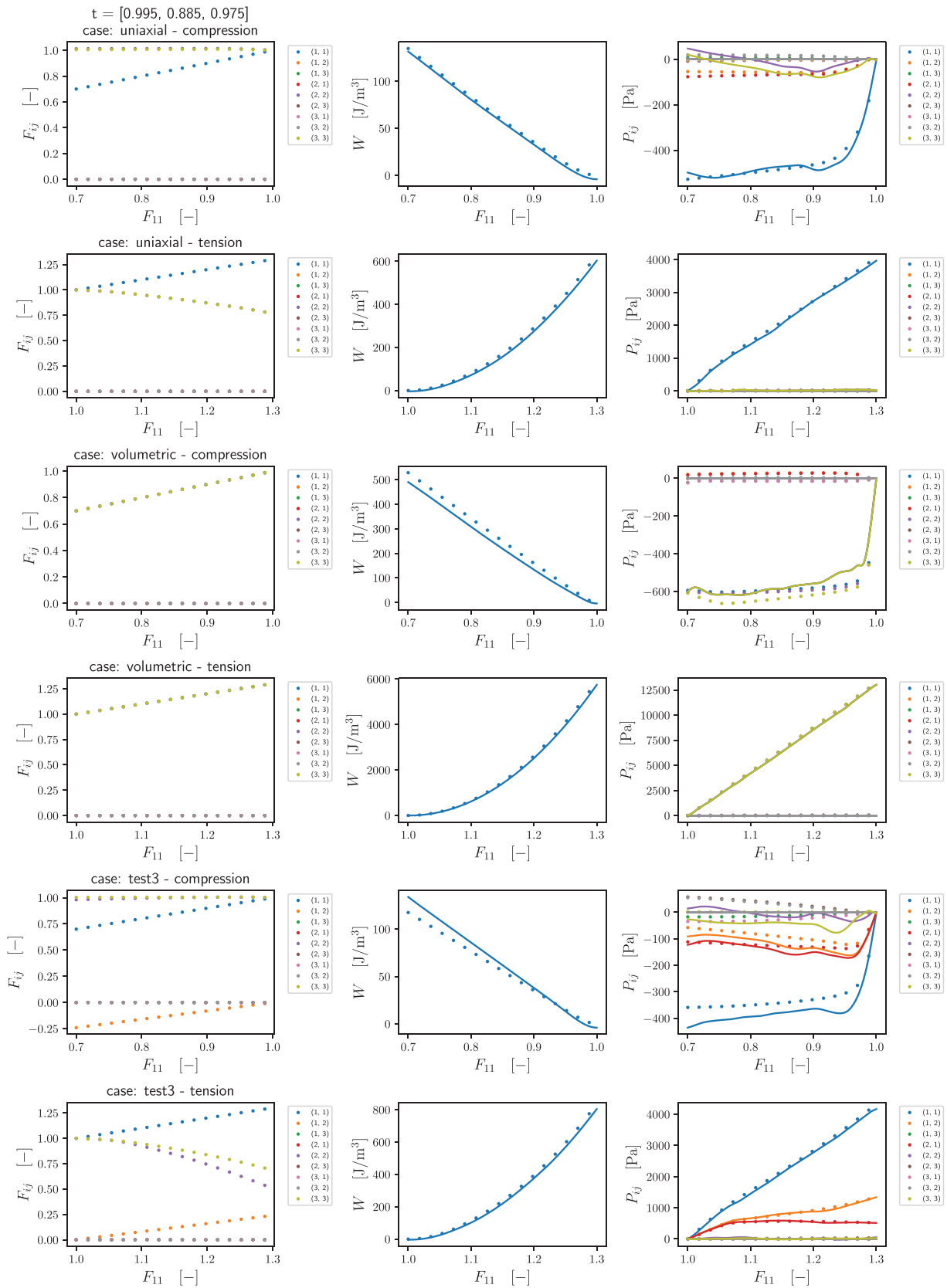


FIGURE A4 Evaluation of trained model \mathcal{M}_u based on network $\mathcal{N}[4,128]$ and $(wMSE^W + wMSE^P)/2$ with uniform weights for $t_2 = (0.995, 0.885, 0.975)$